



HAL
open science

Unveiling the merger dynamics of the most massive MaDCoWS cluster at $z = 1.2$ from a multi-wavelength mapping of its intracluster medium properties

F. Ruppin, M. McDonald, M. Brodwin, R. Adam, P. Ade, P. André, A. Andrianasolo, M. Arnaud, H. Aussel, I. Bartalucci, et al.

► To cite this version:

F. Ruppin, M. McDonald, M. Brodwin, R. Adam, P. Ade, et al.. Unveiling the merger dynamics of the most massive MaDCoWS cluster at $z = 1.2$ from a multi-wavelength mapping of its intracluster medium properties. *The Astrophysical Journal*, 2020, 893 (1), pp.74. 10.3847/1538-4357/ab8007. hal-02410938

HAL Id: hal-02410938

<https://hal.science/hal-02410938v1>



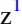

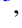

Submitted on 23 Aug 2023

HAL is a multi-disciplinary open access archive for the deposit and dissemination of scientific research documents, whether they are published or not. The documents may come from teaching and research institutions in France or abroad, or from public or private research centers.

L'archive ouverte pluridisciplinaire **HAL**, est destinée au dépôt et à la diffusion de documents scientifiques de niveau recherche, publiés ou non, émanant des établissements d'enseignement et de recherche français ou étrangers, des laboratoires publics ou privés.



Unveiling the Merger Dynamics of the Most Massive MaDCoWS Cluster at $z = 1.2$ from a Multiwavelength Mapping of Its Intracluster Medium Properties

F. Ruppin¹, M. McDonald¹, M. Brodwin² , R. Adam³, P. Ade⁴ , P. André⁵, A. Andrianasolo⁶, M. Arnaud⁵, H. Aussel⁵, I. Bartalucci⁵, M. W. Bautz¹, A. Beelen⁷, A. Benoît⁸, A. Bideaud⁸, O. Bourrion⁹, M. Calvo⁸, A. Catalano⁹, B. Comis⁹, B. Decker², M. De Petris¹⁰, F.-X. Désert⁶, S. Doyle⁴, E. F. C. Driessen¹¹, P. R. M. Eisenhardt¹², A. Gomez¹³, A. H. Gonzalez¹⁴ , J. Goupy⁸, F. Kéruzoré⁹, C. Kramer¹⁵, B. Ladjelate¹⁵, G. Lagache¹⁶, S. Leclercq¹¹, J.-F. Lestrade¹⁷, J. F. Macías-Pérez⁹, P. Mauskopf^{4,18}, F. Mayet⁹, A. Monfardini⁸, E. Moravec¹⁴ , L. Perotto⁹, G. Pisano⁴, E. Pointecouteau¹⁹, N. Ponthieu⁶, G. W. Pratt⁵, V. Revéret⁵, A. Ritacco¹⁵, C. Romero¹¹ , H. Rousset²⁰, K. Schuster¹¹, S. Shu¹¹, A. Sievers¹⁵, S. A. Stanford²¹, D. Stern¹² , C. Tucker⁴, and R. Zylka¹¹

¹ Kavli Institute for Astrophysics and Space Research, Massachusetts Institute of Technology, 77 Massachusetts Avenue, Cambridge, MA 02139, USA
ruppin@mit.edu

² Department of Physics and Astronomy, University of Missouri, 5110 Rockhill Road, Kansas City, MO 64110, USA

³ Laboratoire Leprince-Ringuet, École Polytechnique, CNRS/IN2P3, F-91128 Palaiseau, France

⁴ Astronomy Instrumentation Group, University of Cardiff, UK

⁵ AIM, CEA, CNRS, Université Paris-Saclay, Université Paris Diderot, Sorbonne Paris Cité, F-91191 Gif-sur-Yvette, France

⁶ Univ. Grenoble Alpes, CNRS, IPAG, F-38000 Grenoble, France

⁷ Institut d'Astrophysique Spatiale (IAS), CNRS and Université Paris Sud, Orsay, France

⁸ Institut Néel, CNRS and Université Grenoble Alpes, France

⁹ Univ. Grenoble Alpes, CNRS, Grenoble INP, LPSC-IN2P3, 53, avenue des Martyrs, F-38000 Grenoble, France

¹⁰ Dipartimento di Fisica, Sapienza Università di Roma, Piazzale Aldo Moro 5, I-00185 Roma, Italy

¹¹ Institut de RadioAstronomie Millimétrique (IRAM), Grenoble, France

¹² Jet Propulsion Laboratory, California Institute of Technology, Pasadena, CA 91109, USA

¹³ Centro de Astrobiología (CSIC-INTA), Torrejón de Ardoz, E-28850 Madrid, Spain

¹⁴ Department of Astronomy, University of Florida, 211 Bryant Space Center, Gainesville, FL 32611, USA

¹⁵ Institut de RadioAstronomie Millimétrique (IRAM), Granada, Spain

¹⁶ Aix Marseille Université, CNRS, LAM (Laboratoire d'Astrophysique de Marseille) UMR 7326, F-13388, Marseille, France

¹⁷ LERMA, Observatoire de Paris, PSL Research University, CNRS, Sorbonne Universités, UPMC Univ., F-75014, Paris, France

¹⁸ School of Earth and Space Exploration and Department of Physics, Arizona State University, Tempe, AZ 85287, USA

¹⁹ IRAP, Université de Toulouse, CNRS, CNES, UPS, (Toulouse), France

²⁰ Institut d'Astrophysique de Paris, CNRS (UMR7095), 98 bis boulevard Arago, F-75014, Paris, France

²¹ Department of Physics, University of California, One Shields Avenue, Davis, CA 95616, USA

Received 2019 November 1; revised 2020 March 8; accepted 2020 March 14; published 2020 April 16

Abstract

The characterization of the Intracluster Medium (ICM) properties of high-redshift galaxy clusters is fundamental to our understanding of large-scale structure formation processes. We present the results of a multiwavelength analysis of the very massive cluster MOO J1142+1527 at a redshift $z = 1.2$ discovered as part of the Massive and Distant Clusters of WISE Survey. This analysis is based on high angular resolution Chandra X-ray and NIKA2 Sunyaev–Zel'dovich (SZ) data. The cluster thermodynamic radial profiles have been obtained with unprecedented precision at this redshift and up to $0.7R_{500}$, thanks to the combination of high-resolution X-ray and SZ data. The comparison between the galaxy distribution mapped in infrared by Spitzer and the morphological properties of the ICM derived from the combined analysis of the Chandra and NIKA2 data leads us to the conclusion that the cluster is an ongoing merger. We have estimated a systematic uncertainty on the cluster total mass that characterizes both the impact of the observed deviations from spherical symmetry and of the core dynamics on the mass profile. We further combine the X-ray and SZ data at the pixel level to obtain maps of the temperature and entropy distributions. We find a relatively low-entropy core at the position of the X-ray peak and high-temperature regions located on its south and west sides. This work demonstrates that the addition of spatially resolved SZ observations to low signal-to-noise X-ray data brings a high information gain on the characterization of the evolution of ICM thermodynamic properties at $z > 1$.

Unified Astronomy Thesaurus concepts: Galaxy clusters (584); Sunyaev-Zeldovich effect (1654); X-ray astronomy (1810); High-redshift galaxy clusters (2007); Intracluster medium (858); Cool cores (302)

1. Introduction

Clusters of galaxies form at the intersection of cosmic filaments and grow hierarchically through the joint processes of slow accretion of surrounding material and merger events with substructures (e.g., Press & Schechter 1974). Most of their baryonic matter content is made of a hot and diffuse plasma called the Intracluster Medium (ICM) embedded within a dark-matter halo. As the largest gravitationally bound objects,

galaxy clusters provide a wealth of information on both the history of large-scale structure formation and the dynamics of the universe (e.g., Voit 2005). The characterization of the evolution of the ICM thermodynamic properties with the mass and redshift of galaxy clusters thus gives us a way to test our current models describing the astrophysical processes that play a fundamental role during their growth as well as the underlying cosmology in which these processes take place.

The vast majority of the detailed analyses of ICM astrophysical processes have been focused on $z < 1$ clusters observed primarily in X-ray (e.g., Pratt et al. 2010; Pcaud et al. 2016; Calzadilla et al. 2019; McDonald et al. 2019) and to some extent in SZ (e.g., Mroczkowski et al. 2012; Planck Collaboration et al. 2013). These studies provided valuable constraints on a plethora of mechanisms such as gas cooling, feedback from Active Galactic Nuclei (AGNs), the physics behind cold and shock fronts, and merger dynamics. The comparison of both the amplitude and the shape of the mean radial distributions of ICM properties for representative cluster samples together with results from numerical simulations have enabled improving our understanding of cluster dynamics (e.g., Walker et al. 2012; Pike et al. 2014). Furthermore, knowing the mean ICM thermodynamic properties and how they scale with halo mass and redshift is essential to the use of clusters as cosmological probes (e.g., Planck Collaboration et al. 2016a).

However, the most active formation epoch for clusters with a mass larger than $10^{14} M_{\odot}$ is assumed to lie at redshifts $1 < z < 2$ (e.g., Poole et al. 2007; Fakhouri et al. 2010). During this period, the first bona fide clusters merged with galaxy groups, and extended protoclusters collapsed into more compact and massive halos (e.g., Muldrew et al. 2015). Also at these redshifts, cluster galaxies underwent a high star-formation rate, and an excess in the AGN fraction is found (e.g., Alberts et al. 2016). Furthermore, the mean ICM thermodynamic properties found at low redshift may have significantly evolved since $z \sim 2$, as the merger rate is expected to be much higher at $z \gtrsim 1$ (McDonald et al. 2014). This evolution may result in important modifications of the cosmological constraints issued from the study of cluster abundance (Ruppin et al. 2019). It is therefore essential to probe the ICM properties at redshifts higher than 1 to extend our knowledge of the distant progenitor objects of the most massive clusters at $z \sim 0$.

With the current X-ray observatories, the required exposures to probe the evolution of the radial distributions of all ICM thermodynamic properties at $z > 1$ are extremely long and usually prevent such studies from being realized. Furthermore, X-ray-selected samples may be affected by important selection biases (e.g., Eckert et al. 2011). The past decade has seen the advent of large Sunyaev-Zel'dovich (SZ) surveys capable of detecting massive galaxy clusters up to high redshifts. These include the Planck (Planck Collaboration et al. 2016b), South Pole Telescope (SPT; Bleem et al. 2015), and Atacama Cosmology Telescope (ACT; Hasselfield et al. 2013) surveys, with the latter two extending to $z > 1$. However, the relatively low angular resolution of these instruments precludes these surveys from constraining the shape of the ICM pressure distribution or cluster morphology at high redshift. In contrast, the recently commissioned single-dish SZ instruments MUSTANG-2 (Dicker et al. 2014) and NIKA2 (Calvo et al. 2016; Adam et al. 2018; Perotto et al. 2019) open new possibilities regarding the characterization of the ICM properties even at the highest redshifts. Their high angular resolution ($\sim 9''$ – $18''$) and large field of view ($\sim 5'$ – $7'$) allow us to map the SZ signal over a range of scales that is similar to the X-ray measurements made by the current X-ray observatories such as Chandra and XMM-Newton. Joint SZ and X-ray analyses represent a new frontier in high-redshift cluster studies and promise to address outstanding questions associated with the formation and evolution of the ICM. At low redshifts, such joint studies

have yielded detailed characterization of individual cluster merger dynamics (e.g., Adam et al. 2017a) and radial profiles of the ICM thermodynamic properties without relying on X-ray spectroscopic data (e.g., Ruppin et al. 2017). Furthermore, the comparison between the ICM morphological states derived from X-ray and SZ observations can uncover evidence of ICM disturbances that neither probe is able to highlight independently (e.g., Adam et al. 2014; Ruppin et al. 2018). For the first time, we can characterize all of the ICM thermodynamic properties and the morphology of individual clusters from joint X-ray/SZ analyses at $z > 1$.

The current SZ catalogs do not allow us to define a mass-limited sample of $z > 1$ clusters to be considered for high angular resolution SZ and X-ray follow ups in similar ranges of angular scales. The SPT clusters ($\delta < -20^{\circ}$) cannot be observed by MUSTANG-2 nor by NIKA2, and the $z > 1$ ACT clusters have an average decl. of $-2^{\circ}.5$, which is also too low to perform efficient SZ observations with these instruments. Furthermore, the Atacama Large Millimeter/submillimeter Array and the Atacama Compact Array interferometers strongly filter the large-scale SZ signal. They are therefore not adapted to probe the outer regions of the ICM in reasonable exposure times (e.g., Kitayama et al. 2016).

The current generation of Infrared (IR)-selected galaxy-based cluster searches complements the work of past millimeter surveys, exploring large volumes of the universe to detect the rarest high-mass and high- z clusters. The Massive and Distant Clusters of WISE Survey (MaDCoWS) has been designed to detect the most massive galaxy clusters at $z \gtrsim 1$ (Gonzalez et al. 2018). It offers the largest survey area among current high-redshift cluster searches, using infrared and optical imaging from the Wide-field Infrared Survey Explorer (WISE; Wright et al. 2010) and the Panoramic Survey Telescope and Rapid Response System (Chambers et al. 2016) to robustly isolate galaxy clusters at $z \gtrsim 1$ over more than 80% of the extragalactic sky. The combination of high angular resolution SZ observations from NIKA2 or MUSTANG-2 with X-ray data measured in the direction of MaDCoWS clusters offers an ideal opportunity to characterize the ICM evolution at $1 < z < 2$.

In this paper, we present a multiwavelength analysis of the MaDCoWS cluster MOO J1142+1527 at $z = 1.19$ confirmed in SZ by Gonzalez et al. (2015) using the Combined Array for Research in Millimeter-wave Astronomy (CARMA). These previous SZ observations have shown that MOO J1142+1527 is the most massive cluster known at $z > 1.15$ with a mass $M_{500} = (6.0 \pm 0.9) \times 10^{14} M_{\odot}$. By combining spatially resolved X-ray and SZ observations from Chandra and NIKA2, we can, for the first time, estimate the radial profiles of all ICM thermodynamic properties, map their average values along the line of sight, and study the relation between the spatial distribution of these properties and cluster morphology at $z > 1$. We describe both the NIKA2 observations and raw data analysis in Section 2. We characterize the radio-source contamination of the SZ signal in the NIKA2 data in Section 3. In Section 4, we give the details of the Chandra observations and the X-ray data reduction. We study the cluster morphology based on our multiwavelength data set in Section 5. We combine the X-ray and SZ data to estimate the radial profiles of the ICM thermodynamic properties in Section 6. In Section 7, maps of the ICM temperature and entropy are obtained from the combination of the Chandra and NIKA2 data at the pixel level. We present our perspectives

given the results of this study in Section 8 and give a summary of our work in Section 9. In this paper, we assume a Λ CDM cosmology based on the latest results from the Planck collaboration (Planck Collaboration et al. 2018).

2. NIKA2 SZ Observations

This section presents the details of the NIKA2 SZ observations of MOO J1142+1527 completed in 2017 October. We first briefly review the main properties of the thermal SZ effect. We then describe the conditions of the data acquisition as well as the different steps of the raw data analysis. We estimate both the residual noise properties and SZ signal filtering and finally characterize the cluster morphology based on the NIKA2 SZ surface brightness maps.

2.1. The Thermal Sunyaev–Zel’dovich Effect

The thermal SZ effect (tSZ; Sunyaev & Zel’dovich 1972, 1980) corresponds to a variation of the apparent brightness of the cosmic microwave background (CMB) due to the inverse Compton scattering of CMB photons on energetic electrons within any reservoir of hot plasma along the line of sight:

$$\frac{\Delta I_{\text{tSZ}}}{I_0} = y_{\text{tSZ}} f(\nu, T_e), \quad (1)$$

where $f(\nu, T_e)$ characterizes the frequency dependence of the tSZ spectrum (Birkinshaw 1999; Carlstrom et al. 2002) and T_e is the electronic temperature of the plasma. The Compton parameter y_{tSZ} gives the amplitude of the spectral distortion in the direction \hat{n} . It is expressed as

$$y_{\text{tSZ}}(\hat{n}) = \frac{\sigma_{\text{T}}}{m_e c^2} \int P_e dl, \quad (2)$$

where m_e is the electron mass, c is the speed of light, σ_{T} is the Thomson scattering cross section, and P_e is the electron pressure distribution of the gas. Being almost redshift independent,²² the thermal SZ effect allows us to directly measure the ICM pressure distribution up to high redshifts. It depends only mildly on the ICM temperature through the relativistic corrections to the tSZ spectrum (Itoh et al. 1998; Pointecouteau et al. 1998). More details can be found on the information gain brought by spatially resolved SZ observations to probe ICM astrophysics in the review of Mroczkowski et al. (2019).

2.2. NIKA2 Observations and Data Reduction

We conducted spatially resolved SZ observations of MOO J1142+1527 in 2017 October with the NIKA2 camera (OpenTime: 082-17, PI: F. Ruppín) installed at the Institut de Radioastronomie Millimétrique (IRAM) 30 m telescope. We have observed this cluster for an effective time of 10.4 hr. The pointing center was chosen to be (R.A., decl.)_{J2000} = (11:42:46.6, +15:27:15.0) according to the estimate of the SZ centroid position found by Gonzalez et al. (2015) using CARMA. We defined the scanning strategy in a similar way as the one presented in Adam et al. (2015) and Ruppín et al. (2017). A succession of on-the-fly raster scans of 8×4 arcmin² with 10'' steps between each subscan has been

realized in four different directions in equatorial coordinates (J2000) at a scanning speed of 40 arcsec/s. The cluster has been observed at a mean elevation of 55°.4. The weather conditions at the time of the observations were quite good with a mean zenith opacity of 0.19 at 150 GHz, 0.32 at 260 GHz, and a rather stable atmosphere.

We use Uranus as a primary calibrator of the data. Following the baseline calibration procedure described in Perotto et al. (2019), we obtain total calibration uncertainties of 6% and 8% at 150 and 260 GHz, respectively. These estimates take into account the absolute calibration uncertainty of 5% on the Uranus flux density expectations reported in Moreno (2010). The distribution of pointing corrections realized at regular intervals during the observations of MOO J1142+1527 is characterized by a mean of 1''9 and a standard deviation of 1''2. More details on the instrumental performance of the NIKA2 camera at the time of the observations can be found in Adam et al. (2018) and Perotto et al. (2019).

The selection of valid detectors and the removal of cryogenic vibrations and cosmic-ray glitches from the raw data have been realized following the pre-processing method detailed in Adam et al. (2015). We removed the spatially correlated noise contaminants induced by both the atmospheric emission and the electronic readout system using an iterative procedure similar to the one described in Ruppín et al. (2018). The data measured by each array are treated separately. For each detector timeline, a contaminant template is defined as a combination of a common mode computed using all of the valid detectors in the considered array, a common mode estimated across the timelines of detectors sharing the same readout electronic board, and the elevation path of the detector in the plane of the sky. This allows us to simultaneously model the atmospheric and electronic contaminants as well as the timeline drift induced by air mass variations during the scan. At the end of each iteration, we locate the map pixels with a signal-to-noise ratio (S/N) higher than 4 and remove the corresponding signal amplitude in each detector timeline before the common mode estimations of the next iteration. This allows us to reduce the bias induced by the SZ signal on the estimate of the contaminant templates. The filtering of the SZ signal is therefore reduced at each iteration. We stop the iterative procedure when the variation of the SZ peak amplitude caused by this decrease of the signal filtering is lower than 0.1%. This corresponds to a total of 13 iterations of the raw data analysis. We project the processed timelines onto two different pixelized grids. The first one is defined by a pixel size of 0''984 equal to the one considered in the Chandra analysis described in Section 4. This allows us to directly combine the NIKA2 and Chandra maps in Section 7 in order to estimate the projected distributions of the cluster thermodynamic properties. For the second one, we use a pixel size of 3'' in order to increase the computing efficiency of the SZ deprojection procedure described in Section 6 without significantly degrading the NIKA2 angular resolution at 150 and 260 GHz. All of the individual scans are finally coadded using an inverse variance noise weighting of the data samples in each pixel to obtain the final maps shown in Figure 1.

The methodology applied to estimate the contaminant templates based on two different common modes allows us to significantly reduce the amount of residual-correlated noise in the final maps. The residual noise power spectrum has been estimated based on null maps computed from the

²² In practice, the observation of high-redshift sources with the SZ effect is only limited by the instrumental beam dilution.

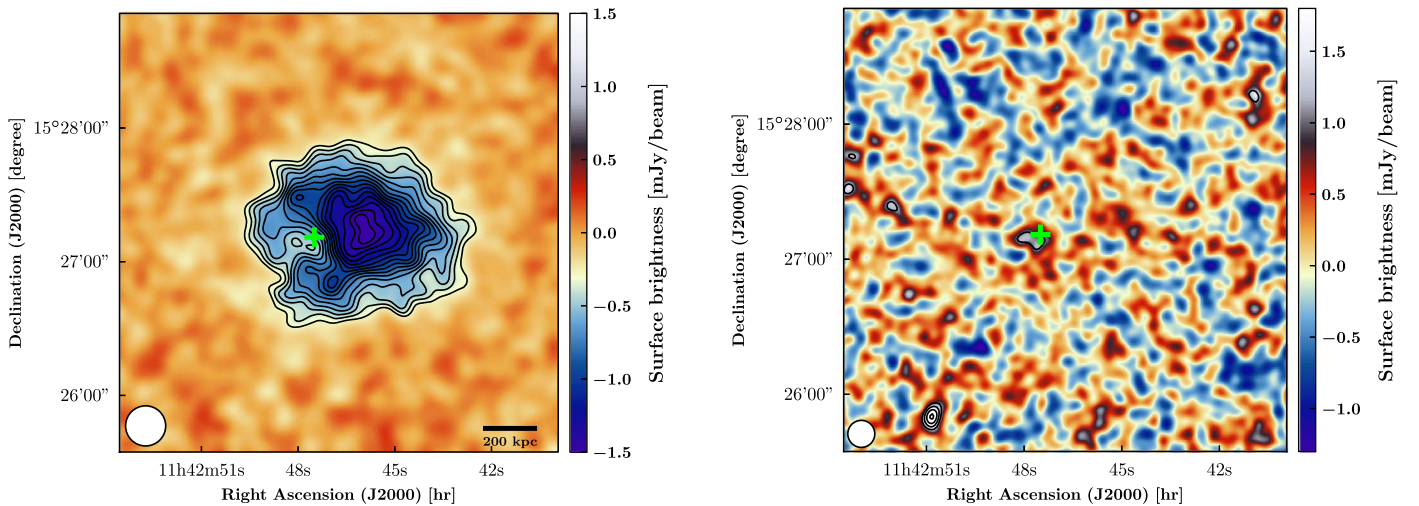


Figure 1. NIKA2 surface brightness maps of MOO J1142+1527 at 150 GHz (left panel) and 260 GHz (right panel). The maps are smoothed with an additional $8''$ and $5''$ Full Width at Half Maximum (FWHM) Gaussian filter at 150 and 260 GHz, respectively, for display purposes. The significance contours in black start at 3σ with steps of 1σ . We represent the width of the NIKA2 beams as white disks in the bottom left-hand corner of the maps. The considered FOV is $3.3'$ wide. The green cross in both panels gives the location of the radio source identified in the FIRST survey.

semi-difference of coadded scans issued from two equivalent subsamples following the procedure described in Adam et al. (2016) and Ruppin et al. (2018). The noise power spectra measured at 150 and 260 GHz are fitted by a model defined as the sum of a white-noise component and a power law to account for the spatial correlations of the residual noise. Although the power-law model obtained at 260 GHz significantly differs from being constant, we find that the noise power spectrum measured at 150 GHz is well modeled by a simple white-noise component. For this reason, the diagonal elements of the noise correlation matrix at 150 GHz dominate over non-diagonal ones. We can therefore assume that the error associated with the signal measured in the map pixels at 150 GHz is given by the root mean square (rms) value in each of them. This results in a significant decrease of the computation time of the deprojection procedure detailed in Section 6.

This significant improvement in the correlated contaminant removal comes at the cost of a high filtering of the extended SZ signal at S/Ns lower than the 4σ threshold used in the iterative analysis of the raw data. We compute the circular transfer function resulting from the NIKA2 observations and data processing at 150 GHz using simulations as described in Adam et al. (2015). We find that the SZ signal filtering is on average 17% larger than the one resulting from the analysis procedure described in Ruppin et al. (2018) in the range of angular scales that can be constrained by NIKA2, i.e., $[0.25-6.5]$ arcmin. However, the SZ map obtained at 150 GHz in Ruppin et al. (2018) was significantly contaminated by spatially correlated residual noise. In this paper, we choose to favor an analysis method that allows us to simultaneously measure a nearly flat noise power spectrum at 150 GHz and an extension of the region where the SZ signal is significant that is already larger than the one where the X-ray signal measured by Chandra is significantly different from the background. This allows us to maximize the S/N in the maps of the ICM temperature and entropy obtained in Section 7.

2.3. NIKA2 Maps of MOO J1142+1527

The surface brightness maps of MOO J1142+1527 obtained at the end of the analysis of the NIKA2 data at 150 and 260 GHz are shown in Figure 1. They correspond to the grids made of $0.984''$ pixels and centered on the SZ peak coordinates measured by CARMA (Gonzalez et al. 2015). For visual purposes, we have smoothed the maps with an additional $8''$ and $5''$ FWHM Gaussian filter at 150 and 260 GHz, respectively. We measure the rms noise at the map center to be $98 \mu\text{Jy}/\text{beam}$ and $423 \mu\text{Jy}/\text{beam}$ at these effective resolutions of $20''$ and $13''$ at 150 and 260 GHz, respectively. These estimates have been obtained following the procedure described in Adam et al. (2017a). Simulated noise maps are computed from the NIKA2 residual noise power spectra at 150 and 260 GHz and from astrophysical contaminant models (Béthermin et al. 2012; Planck Collaboration et al. 2014, and Tucci et al. 2011). The latter allows us to take into account the contributions induced by both the cosmic infrared background (CIB) shot noise and clustering and the CMB temperature anisotropies in the residual noise. As the processing methodology adopted to analyze the NIKA2 raw data has enabled the reduction of the amount of residual-correlated noise compared to previous NIKA2 studies, the instrumental and atmospheric noise contributions are comparable to the one induced by CIB shot noise at 150 GHz. We add all of the noise contaminants in quadrature in order to estimate the S/N in each map pixel at 150 and 260 GHz.

We observe a significant negative SZ signal in the NIKA2 map at 150 GHz shown in the left panel of Figure 1. The SZ peak is found at a position of $(\text{R.A.}, \text{decl.})_{\text{J2000}} = (11:42:45.9, +15:27:12.0)$ with a significance of 17σ at $\sim 10''$ from the pointing center. We compute the SZ surface brightness profile from the NIKA2 map at 150 GHz and measure an S/N higher than 3 up to $1.1'$ away from the SZ peak. This is comparable to the extension of the diffuse X-ray emission recovered by Chandra as described in Section 4. We find some evidence of an elliptical morphology of the SZ signal with an east-west orientation. We fit the 3σ S/N contour with an ellipse and

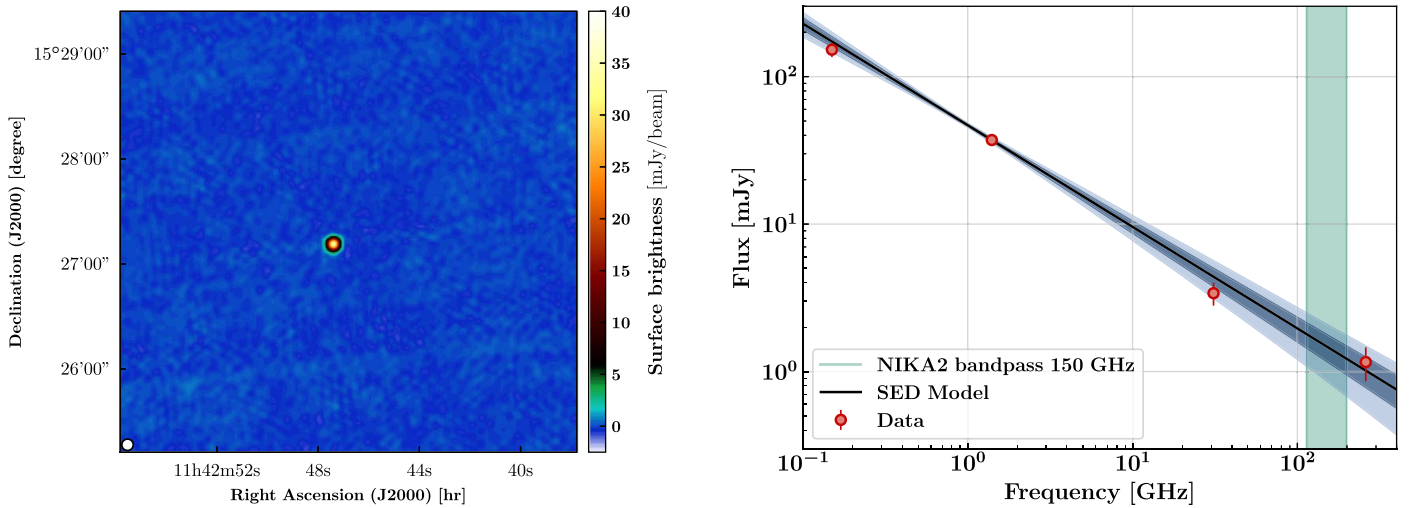


Figure 2. Left panel: surface brightness map of the MOO J1142+1527 sky region obtained by the FIRST survey at 1.4 GHz. A single radio source is detected in the field considered in this paper. Right panel: spectral energy distribution (SED) of the radio source shown in the left panel. The red data points correspond to the TGSS, FIRST, CARMA, and NIKA2 260 GHz flux measurements at different frequencies. The black line is our best-fit SED model. The dark and light blue shaded regions give the 1σ and 2σ confidence intervals. The green band indicates the range of frequencies covered by NIKA2 at 150 GHz.

Table 1
Location of the Radio Source Detected in a $4'$ Radius Circular Region Centered on MOO J1142+1527

Position	153 MHz (mJy)	1.4 GHz (mJy)	31 GHz (mJy)	260 GHz (mJy)
$11^{\text{h}}42^{\text{m}}47^{\text{s}}.421 + 15^{\text{d}}27^{\text{m}}11^{\text{s}}.48$	152.3 ± 16.6	37.17 ± 0.20	3.4 ± 0.6	1.2 ± 0.3

Note. We report its flux densities measured at different frequencies by the TGSS (Intema et al. 2017) and FIRST (Becker et al. 1995) surveys as well as the CARMA (Gonzalez et al. 2015) and NIKA2 observations of the cluster.

measure a flattening $f = 1 - b/a = 0.19$ where a and b are the major and minor axis length, respectively. This is consistent with the SZ morphology found by CARMA (Gonzalez et al. 2015). However, the NIKA2 instrumental performance allows us to further resolve the ICM structure. This will enable constraining the radial pressure profile in Section 6.

We do not detect any significant SZ signal in the NIKA2 260 GHz map shown in the right panel of Figure 1 as anticipated given the expected SZ signal and the noise level at this frequency. Based on the value of the peak SZ surface brightness at 150 GHz, the tSZ spectrum analytic expression, and the NIKA2 bandpasses at the time of the observation, the expected value of the peak SZ surface brightness at 260 GHz is found to be $540 \mu\text{Jy}/\text{beam}$. This corresponds to 1.3 times the rms noise found at the NIKA2 map center at this frequency. However, we detect several point sources in the NIKA2 map at 260 GHz including one within the region where a significant SZ signal is measured at 150 GHz. This source is detected at $25''$ to the east of the NIKA2 SZ peak at 150 GHz. This position is consistent with a radio source found in the Faint Images of the Radio Sky at Twenty-Centimeters survey (FIRST; Becker et al. 1995), which covers the northern sky at 1.4 GHz. We highlight this position with a green cross in both NIKA2 maps in Figure 1. The signal emitted by this source is partly compensating for the negative SZ signal induced by MOO J1142+1527 at 150 GHz. This explains the origin of the hole in the SZ signal found at this position in the NIKA2 map. For this reason, it is essential to estimate the expected flux of this source at 150 GHz before constraining the

ICM pressure profile from a deprojection of the NIKA2 data to minimize the bias induced by this contaminant.

3. Point-source Contamination

This section is dedicated to the study of the point-source contamination of the SZ signal measured in the NIKA2 map at 150 GHz (see Section 2.3). This work will allow us to jointly fit the SZ signal and the point-source emission in order to accurately estimate the ICM pressure profile in Section 6 (e.g., Sayers et al. 2013).

As shown in the left panel of Figure 2, a single radio source has been detected by the FIRST survey at 1.4 GHz in the region observed by NIKA2 (Becker et al. 1995). This source is located on the east side of the SZ peak of MOO J1142+1527 at the same location of the X-ray peak emission measured by Chandra (see Section 4). Its location also coincides with that of the brightest cluster galaxy (BCG) observed in infrared by Spitzer (see Section 5). We therefore conclude that this radio source is hosted by the BCG. The flux of this source has also been measured at 153 MHz by the TIFR GMRT Sky Survey (TGSS; Intema et al. 2017) and at 31 GHz by CARMA (Gonzalez et al. 2015). We measure the flux of this source in the NIKA2 map at 260 GHz by fitting a 2D Gaussian function at the source location found by FIRST using an FWHM fixed to the NIKA2 angular resolution at this frequency. We report our result along with the previous flux measurements of this source in Table 1. Following the methodology developed in Adam et al. (2016), we estimate the expected flux of this radio

source at 150 GHz by fitting its spectral energy distribution (SED) based on the available flux measurements. We use a power-law model given by

$$F_\nu = F_{1\text{ GHz}} \left(\frac{\nu}{1\text{ GHz}} \right)^{\alpha_{\text{radio}}} \quad (3)$$

where $F_{1\text{ GHz}}$ gives the SED amplitude at a reference frequency of 1 GHz and α_{radio} is the SED spectral index. The four data points shown in red in the right panel of Figure 2 are used to obtain the best-fit values of these two parameters, i.e., $(F_{1\text{ GHz}}, \alpha_{\text{radio}}) = (46.8\text{ mJy}, -0.69)$, and their associated covariance at maximum likelihood. We simulate mock SEDs using a Gaussian sampling of the parameter space around the best-fit values based on the parameter covariance. The best-fit SED model is shown with the black line in Figure 2 along with its associated 1σ and 2σ confidence intervals in dark and light blue obtained from the simulated SEDs. Each mock SED is integrated in the NIKA2 bandpass at 150 GHz. The mean and standard deviation of all of the realizations give us an estimate of the expected flux of the radio source at this frequency, $F_{150\text{ GHz}} = 1.5 \pm 0.3\text{ mJy}$. We use this result to define a Gaussian prior on the source emission at 150 GHz in Section 6.

There is no available ancillary data on the contamination induced by submillimeter galaxies in the considered sky region. However, based on the NIKA2 data at 260 GHz, we find no submillimeter sources with a flux high enough to be detected within the region where a significant SZ signal is measured at 150 GHz. We therefore consider this contaminant to be negligible in the following sections. We note however that a submillimeter galaxy is detected at 260 GHz with an S/N of 6 at a position of (R.A., decl.)_{J2000} = (11:42:50.8, +15:25:50.4), i.e., at ~ 2.1 from the SZ peak at 150 GHz. We compute the ratio between the fluxes measured at this position at 150 and 260 GHz and find a value of $F_{150\text{ GHz}}/F_{260\text{ GHz}} = 0.1$. This is consistent with the ratios found for the population of dusty galaxies detected at 150 and 214 GHz by the SPT (Vieira et al. 2010).

4. Chandra X-Ray Observations

This section presents the X-ray analysis of the Chandra observations of MOO J1142+1527 realized during Cycle 17 in 2017 February (ObsID: 18277, PI: A. Stanford). We first review the main steps of the raw data analysis aimed at obtaining both the background and point-source-subtracted event list, as well as the X-ray spectrum in the region of interest. We further present the analysis of these data products in order to measure the cluster X-ray surface brightness profile and its mean spectroscopic temperature.

4.1. Observations and Data Reduction

The X-ray observations of MOO J1142+1527 were obtained in the VFAINT data mode for a total exposure of 46.96 ks using the Advanced CCD Imaging Spectrometer (ACIS)-I chips on board the Chandra X-ray Observatory. We follow the data reduction procedure described in McDonald et al. (2017) and references therein. We have reduced the data using the Chandra Interactive Analysis of Observations (CIAO) software v4.10 based on the calibration database (CALDB) v4.8.0

provided by the Chandra X-ray Center (CXC). We have used the `chandra_repro` script to reprocess the level 1 event files using the latest charge transfer inefficiency corrections and time-dependent gain adjustments. The ACIS particle background for very faint mode observations is also cleaned based on outer pixel pulse heights during this analysis step. We use the `lc_clean` routine based on M. Markevitch's program (Markevitch 2001) to remove flares from light curves created with a temporal bin size of 259.28 s. We find a total, cleaned exposure time of 46.19 ks.

The exposure map associated with the observations has been computed in an energy band restricted from 0.5 to 7 keV and a center-band energy of 2.3 keV as recommended by the CXC. Point sources have been identified using the `wavdetect` script based on a wavelet decomposition technique (e.g., Vikhlinin et al. 1998). We also perform a visual inspection of the regions enclosing the detected sources. A mask has been generated using the resulting list of point sources. It is used in Section 4.2 to produce a cleaned event list from which the X-ray surface brightness profile as well as the X-ray spectrum are extracted. We define the X-ray background as a combination of (1) a particle and instrumental background, and (2) a local astrophysical background. For the particle and instrumental background, we normalize unscaled stowed background files to the count rate observed in the 9–12 keV band. The significant diffuse emission from the cluster has only been detected by the I3 chip. The remaining three ACIS-I chips are therefore used as an estimate of the local astrophysical background once both particle background and point sources have been removed.

We show an exposure-corrected map of the Chandra observations of MOO J1142+1527 after background and point-source subtraction in the left panel of Figure 3. The diffuse X-ray emission is significantly detected within a region of similar angular scale as the one obtained with the NIKA2 SZ observations (see Figure 1). The X-ray peak (blue cross) is detected at the same location as the radio source observed in the FIRST map in the left panel of Figure 2. We note that a careful analysis has been made in order to show that the X-ray peak is not contaminated by an X-ray point source but is really caused by an over-density within the ICM. In particular, the `wavdetect` routine has been used in different energy intervals within the soft and hard bands to confirm that no X-ray point source is detected at the X-ray peak position. Therefore, together with the results obtained on the radio emission of the central AGN in Section 3, we find that the latter has an X-ray luminosity compatible with 0 and a radio luminosity at 1.4 GHz of $L_{1.4\text{ GHz}} = (1.373 \pm 0.007) \times 10^{25}\text{ W Hz}^{-1}$. This clearly indicates that the BCG hosting the AGN is a member of the corona class and should have an X-ray cool core according to Sun (2009). The cluster emission is clearly elongated westward with respect to the X-ray peak. For this reason, the large-scale morphology of the cluster is similar to the one observed in the NIKA2 map at 150 GHz (see Section 2.3).

As the X-ray emission is clearly not azimuthally symmetric, we choose to use both the cluster large-scale centroid and the X-ray peak for all estimates shown in this paper unless otherwise noted. The centroid position is computed iteratively within a circular region of $1'$ radius centered on the last estimate of the centroid location. We initialize this position to the X-ray peak one. A comparison between the locations of the

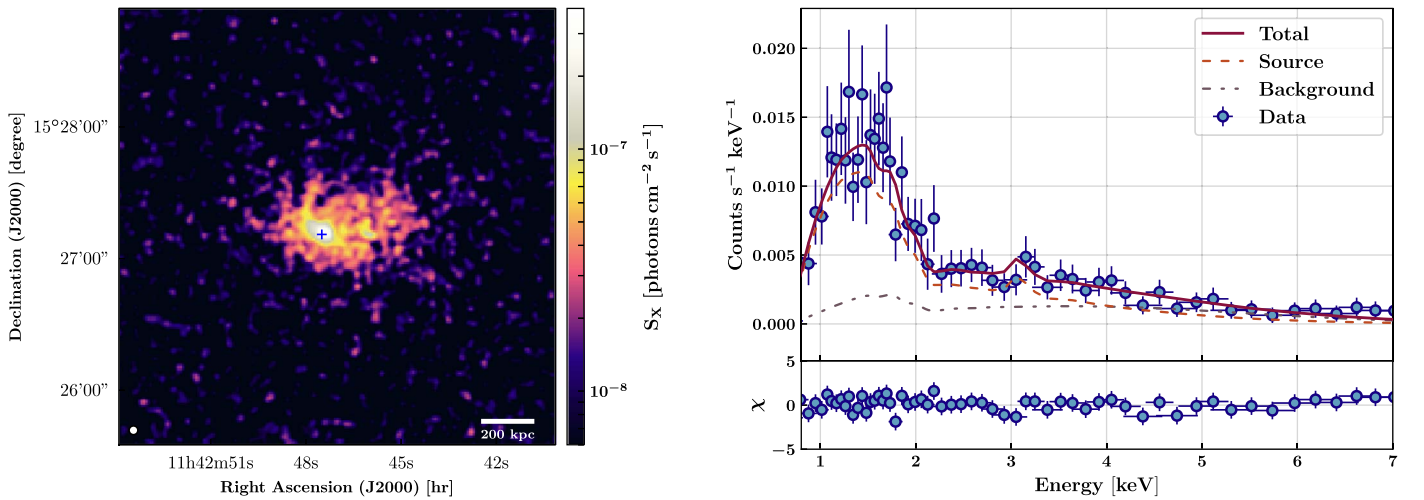


Figure 3. Left panel: exposure-corrected Chandra flux map of MOO J1142+1527 in the 0.7–7.0 keV band. We have binned the event list using $0''.984$ pixels. The image has been smoothed with an additional $3''$ FWHM Gaussian filter, and the colors are displayed with a logarithmic scaling for display purposes. The blue cross gives the location of the radio source characterized in Section 3. Right panel: X-ray spectrum extracted from the Chandra event list after subtracting the particle background (blue points) in an annulus centered on the cluster large-scale centroid with inner and outer radii of $0.15R_{500}$ and R_{500} , respectively. The sum of the source model (orange) and the astrophysical-background model (mauve) fitted jointly gives the final model (red). The lower panel shows the ratio between the difference of the data and the model with the uncertainty associated with each data point.

X-ray peak, the X-ray centroid, and the SZ peak is discussed in Section 5.

Following Maughan et al. (2008) and McDonald et al. (2016), we extract the X-ray spectrum in the 0.7–7.0 keV band using the `specextract` script in a core-excised circular annulus centered on the large-scale centroid and mapping the radii $0.15R_{500} < r < R_{500}$. We iteratively estimate the value of R_{500} based on the best-fit value of the spectroscopic temperature T_X (see Section 4.2) and the $M_{500}-T_X$ scaling relation from Vikhlinin et al. (2009), and we find a value of 790 ± 87 kpc. This is compatible with the result obtained with the core-excised scaling relation of Bulbul et al. (2019), i.e., $R_{500} = 916 \pm 127$ kpc. The scaled stowed background files are used to compute the spectrum of the particle background to be subtracted from the measured spectrum. We repeat the same procedure in the remaining three ACIS-I chips to measure the spectrum of the local astrophysical background. The final X-ray spectrum measured in the cluster region is shown with blue points in the right panel of Figure 3. We group the energy channels to obtain an S/N higher than 5 in each bin. This spectrum presents enough statistics to enable estimating the mean spectroscopic temperature of the ICM.

4.2. Mean Spectroscopic Temperature and Surface Brightness Profile

With low-S/N X-ray data, it is not possible to extract a temperature profile. Hence, we evaluate a mean spectroscopic temperature from the fitting of the cluster spectrum shown in the right panel of Figure 3. The cluster spectrum is fitted jointly with the astrophysical-background spectrum using CIAO’s *Sherpa* package. We fit the whole spectrum using a combination of XSPEC models (v12.10.0e; Arnaud 1996) including a single-temperature plasma (APEC; Smith et al. 2001) for the cluster emission, a soft X-ray Galactic background (APEC; $k_B T_X = 0.18$ keV, $Z = Z_\odot$, $z = 0$) combined with a hard X-ray cosmic spectrum (BREMSS; $k_B T_X = 40$ keV) for the astrophysical background, and a Galactic absorption model (PHABS). For the latter, we fix the Galactic column density to the value found by Kalberla et al. (2005) at this latitude:

$n_H = 2.92 \times 10^{20} \text{ cm}^{-2}$. We also fix the cluster redshift to the value estimated from the combination of the Gemini/GMOS, Keck/DEIMOS, and Keck/MOSFIRE spectroscopy measurements presented by Gonzalez et al. (2015), i.e., $z = 1.19$, in the cluster-emission model. We allow the ICM spectroscopic temperature and the different model normalizations to vary in the analysis. Given the cluster redshift, an iron emission line is expected at an energy of ~ 3 keV. As it is not significantly detected in the measured spectrum, we choose to fix the ICM metallicity to $Z = 0.3Z_\odot$.

The best-fit total model is shown by the red line in the right panel of Figure 3. It is given by the sum of the cluster-emission model (orange) and the astrophysical-background model (gray). The lower panel of the figure displays the ratio of the difference between the data and the best-fit model with the measurement uncertainty in each energy bin. We do not measure any deviations larger than 3σ , and no significant systematic effect is identified in these residuals. We measure a reduced χ^2 of 1.15 ± 0.18 for this analysis based on 59 degrees of freedom. We find that the cluster spectroscopic temperature is given by $T_X = 8.63 \pm 1.86$ keV within a radius range $119 < r < 790$ kpc. We find a consistent result if we use the R_{500} estimate obtained with the Bulbul et al. (2019) scaling relation. This single temperature measurement is shown as a blue point in the right panel of Figure 4. It is a key parameter to define the X-ray emission-measure profile of the cluster in Section 6. As has been shown by Bourdin & Mazzotta (2008), the variation of the neutral hydrogen column density across the field of view can have a significant impact on the ICM temperature estimate. Therefore, a second analysis has been done with a free Galactic column density value. The best-fit value of this parameter is found to be $n_H = 14.68 \times 10^{20} \text{ cm}^{-2}$ with an associated ICM temperature of $T_X = 7.75 \pm 2.13$ keV. As the fitted hydrogen column density is much higher than the expected one, the normalization of the cluster model increases to compensate for the absorption that is significant between 0.7 and ~ 2 keV. This explains why we find a lower spectroscopic temperature associated with this increased Galactic absorption. We find a reduced χ^2 of 1.14 ± 0.18 for this second analysis

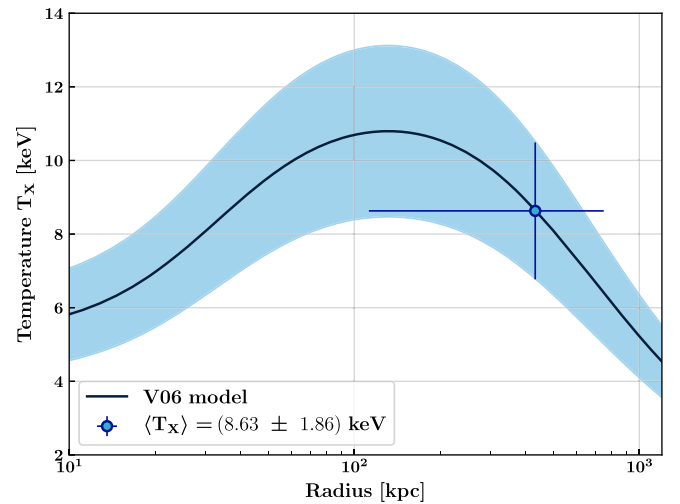
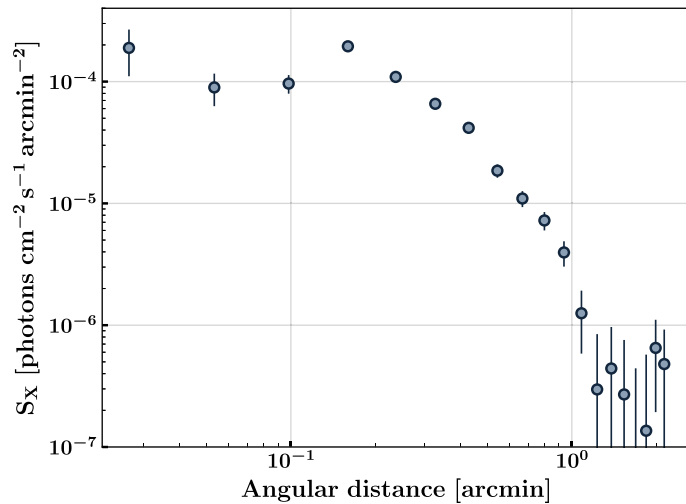


Figure 4. Left panel: Chandra X-ray surface brightness profile extracted within the 20 annuli defined by Equation (4) centered on the cluster large-scale centroid. Right panel: mean ICM spectroscopic temperature estimated from the analysis of the X-ray spectrum measured by Chandra between $0.15R_{500}$ and R_{500} (blue point). The universal temperature model defined by Vikhlinin et al. (2006) scaled to our measurement is shown with a black line, and the blue region gives the 1σ confidence interval.

based on 58 degrees of freedom. Setting the Galactic column density as a free parameter does not significantly improve the spectrum fit. Furthermore, the temperature estimates obtained with the two analyses are compatible, and the fitted value of n_H is in tension with the expected one. Therefore, we choose to keep our first temperature estimate obtained with a fixed hydrogen column density in the sections that follow.

Following the methodology introduced by McDonald et al. (2017), we extract the cluster surface brightness profile in the 0.7–2.0 keV band in 20 annuli defined by

$$r_{\text{out},i} = (a + bi + ci^2 + di^3)R_{500} \quad i = 1 \dots 20 \quad (4)$$

where $(a, b, c, d) = (13.779, 8.8148, 7.2829, 0.15633) \times 10^{-3}$. This definition of the radial binning has been optimized to enable an efficient sampling of the X-ray surface brightness profile of galaxy clusters from Chandra observations up to $z \sim 2$. We use the `dmextract` routine to extract a surface brightness profile from the event list masking the identified point sources. The profile is estimated using both the X-ray peak and the large-scale centroid. We correct the surface brightness profiles for the vignetting effect based on the normalized exposure map estimated in the same energy band. The estimated profile centered on the large-scale centroid is shown in the left panel of Figure 4. The inner slope of the profile is relatively constant, which is expected because the large-scale centroid is offset westward with respect to the X-ray peak location (see Section 5). Significant constraints are established up to an angular distance from the centroid of $\sim 1'.1$, which corresponds to a physical distance of 562 kpc at the cluster redshift. As this detection radius is similar to the one found with the NIKA2 SZ data at 150 GHz, we will highlight it in each figure of the estimated ICM profiles obtained in Section 6. The slight increase in surface brightness observed at an angular distance of $\sim 0'.15$ is due to the X-ray peak brightness averaged in the fourth annuli defined by Equation (4). This Chandra X-ray surface brightness profile along with the spectroscopic temperature estimate are the key

inputs that are considered in Section 6 to deproject the ICM density profile.

5. Multiwavelength Analysis: ICM Morphology

This section aims to describe the morphological properties of MOO J1142+1527 from a multiwavelength comparison of the available data sets. We also infer a possible scenario of the cluster dynamics that would explain the observed cluster morphology in X-ray, optical/infrared, and SZ.

We show a multiwavelength map of MOO J1142+1527 in the left panel of Figure 5. It combines the NIKA2 SZ signal with the point-source subtracted (blue), the galaxy distribution observed at $3.6 \mu\text{m}$ by the Infrared Array Camera (IRAC) on board Spitzer (red), and the Chandra X-ray count isocontours (white). The X-ray peak emission is located at the same position as the radio source shown in Figure 2 and is marked by a magenta square. The X-ray large-scale centroid (see Section 4.1) is found at a distance of ~ 100 kpc westward (yellow circle). The angular separation between these two positions is a clear indication of morphological disturbance.

The location of the SZ peak found by NIKA2 at 150 GHz depends strongly on the estimate of the radio-source flux considered to obtain the point-source-subtracted map and on the residual noise fluctuations at the map center. For this reason, we have generated 1000 realizations of cleaned SZ maps based on the NIKA2 map shown in the left panel of Figure 1 and different estimates of the radio-source flux given the constraints obtained in Section 3. We have also added a noise map realization to each cleaned SZ map based on the rms noise measured at 150 GHz (see Section 2.3). These simulated SZ maps are therefore characterized by an rms noise increased by a factor $\sqrt{2}$ with respect to the NIKA2 SZ map at 150 GHz shown in the left panel of Figure 1. The closed region delimited by an orange dashed-dotted line in Figure 5 contains all locations where the SZ peak is found for at least 95% of all realizations. It contains both the X-ray peak emission and large-scale centroid. The SZ peak found in the NIKA2 raw map at 150 GHz is shown by a cyan diamond. The one measured with

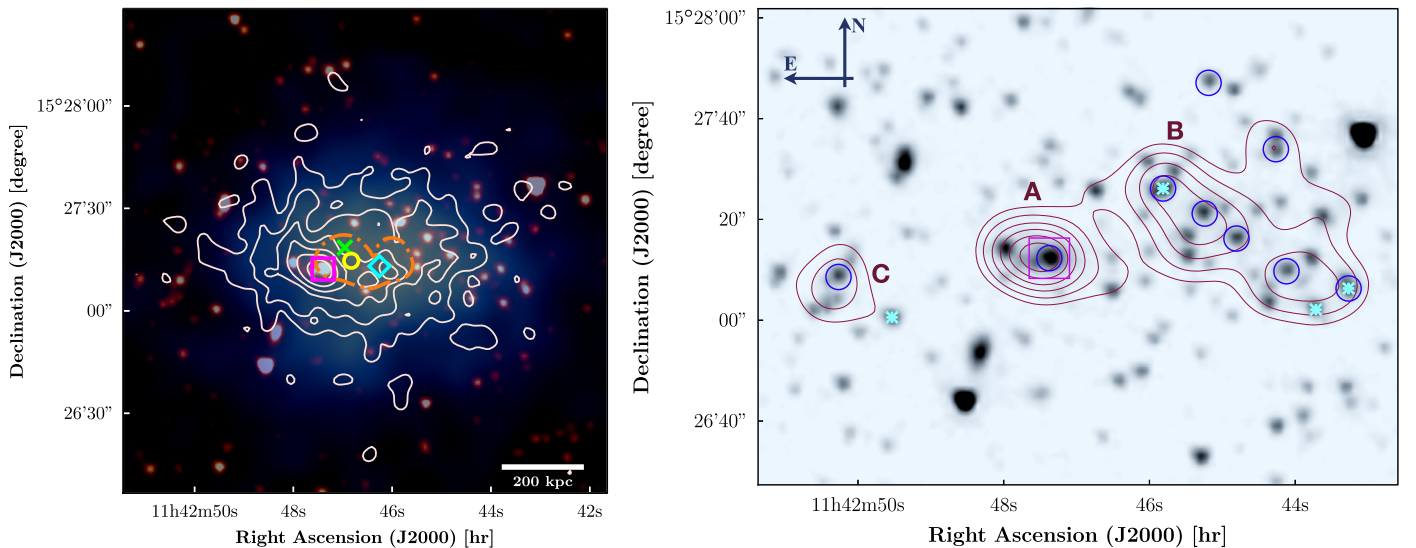


Figure 5. Left panel: multiwavelength map of MOO J1142+1527 showing the Chandra X-ray count isocontours (white), the NIKA2 SZ signal measured at 150 GHz (blue), and the galaxy distribution from IRAC [3.6] (red). The SZ peak location before the point-source subtraction is shown with the cyan diamond. The SZ peak location after subtracting the source-signal contamination is shown by the green cross. The closed area delimited by an orange dashed-dotted line gives the 95% confidence region where the SZ peak is found given the uncertainty on the radio-source flux and the residual noise fluctuations in the NIKA2 map. The yellow circle gives the position of the large-scale X-ray centroid measured by Chandra. Right panel: IRAC [3.6] galaxy distribution in the MOO J1142+1527 field. The red contours give the density peaks in the galaxy distribution. The main peaks are labeled ‘A’, ‘B’, and ‘C’. The cyan stars give the location of spectroscopic cluster members, and the blue circles show the locations of individual WISE sources identified as candidate $z > 0.75$ galaxies. In both panels, the magenta square simultaneously gives the location of the Chandra X-ray peak, the FIRST radio source, and the IRAC brightest cluster galaxy.

the point-source-subtracted map considering a radio-source flux of 1.5 mJy is given by the green cross.

The conclusion of this study is twofold. First, we show that the highest ICM thermal pressure is reached within a region that extends over ~ 230 kpc along the R.A. axis. Although part of this $27''$ extension is due to the NIKA2 angular resolution, this is a clear sign of dynamical disturbance in the cluster core. Indeed, the SZ peak location in clusters with a well-defined core is usually found with a $< 5''$ precision with NIKA2 (e.g., Ruppin et al. 2018). Second, the thermal pressure excess is almost always found to the west of the X-ray peak. This may imply that the maximum thermal pressure value is not due to a maximum ICM electron density but to a gas temperature excess at this location.

We show contours of the IRAC galaxy-density distribution observed in this field in the right panel of Figure 5 (red lines). They have been obtained by smoothing the IRAC image with a $10''$ FWHM Gaussian kernel, masking the brightest foreground sources. Sources identified as candidate $z > 0.75$ galaxies from the WISE color, magnitude, and quality cuts are highlighted with the blue circles, and spectroscopically confirmed cluster members are represented by the red and magenta squares (Gonzalez et al. 2015). The main galaxy-density peak is labeled ‘A’. It coincides with the location of the Chandra X-ray peak, and it contains the BCG (magenta square). A second peak in the spatial distribution of cluster galaxies is found to the west of the thermal pressure excess estimated from the NIKA2 data. It is labeled ‘B’ in this figure. We note that a small group of galaxies, labeled ‘C’, is found to the east of the X-ray peak but is not associated with any X-ray or SZ signal in the Chandra and NIKA2 map at 150 GHz. The combination of all of the features found from this multiwavelength analysis of the cluster morphology leads us to the conclusion that MOO J1142+1527 is an ongoing merger.

A possible explanation for all of the morphological features observed in Figure 5 would be that an infalling subcluster

associated with the second peak in the galaxy distribution (B) is merging through the main halo centered on the BCG (A) from the northwest to the southeast regions of the ICM. Such a merger event would shock-heat the gas and induce both a thermal pressure excess and an elongation of the gas distribution to the west of the main halo core. We favor an ongoing merger scenario in contrast with a post-merger one because the second galaxy-density peak is observed at the same location as the northwest ICM extension. As galaxies are collisionless and the gas is not, we would measure significant differences between the morphology of the ICM and the galaxy distribution if the infalling galaxy group had already passed through the cluster core (Markevitch et al. 2004). Furthermore, we measure a relatively low central entropy and cooling time at the position of the BCG (see Section 6.3). Thus, the cluster core does not seem to have undergone a major merger yet. We note however that this merger does not have to be supersonic to be consistent with the observations. As shown in Section 6, we do not detect any pressure discontinuity in the ICM of MOO J1142+1527, and the NIKA2 angular resolution is not high enough to identify a shock region to the west of the X-ray peak at this redshift. The elongated pressure distribution in the NIKA2 SZ map at 150 GHz is thus consistent with a subsonic ICM disturbance.

6. Multiwavelength Analysis: ICM Profiles

This section is dedicated to the analysis of the radial distributions of the ICM thermodynamic properties of MOO J1142+1527. We use the complementarity of the Chandra X-ray data and the NIKA2 SZ observations in order to estimate both the cluster electron-density profile and its pressure profile. This allows us to precisely measure the temperature and entropy distributions within the ICM under the assumption of spherical symmetry. We also study the effect of the cluster ellipticity and disturbed dynamics on the mass

profile estimated under the assumption of hydrostatic equilibrium.

6.1. Chandra Density Profile

We first describe the methodology followed to estimate the ICM density profile and present our results.

6.1.1. Method

We measure the ICM electron-density profile $n_e(r)$ from the cluster-emission integral given by

$$\text{EI} \equiv \int n_e n_p dV \quad (5)$$

where n_p is the proton density within the ICM, and V is the volume. The emission integral is related to the cluster surface brightness profile through the cooling function computed in the same energy band, $\Lambda(T, Z)$, depending on the ICM temperature T and metallicity Z . We take into account the effects of the Galactic absorption and the variations of the effective area as a function of energy and position in the field of view to measure the cooling function. This is done by computing the normalization factor of the APEC model associated with the cluster spectrum in each annulus considered for the extraction of the surface brightness profile. This normalization factor is associated with a count rate R measured in the annulus of area A , and it depends on both the ICM temperature and the effective area at this position. It is given by

$$\text{norm}(R, A) = \frac{10^{-14}}{4\pi[d_A(1+z)]^2} \int n_e n_p d\Omega dl \quad (6)$$

where d_A is the angular diameter distance, and $d\Omega$ and dl are the solid angle and line-of-sight differential elements, respectively. We therefore compute the conversion coefficient between emission integral and surface brightness at each projected distance from the cluster center. We further correct this estimate for the spatial variations of the ICM temperature assuming a universal temperature profile from Vikhlinin et al. (2006) normalized to the mean spectroscopic temperature T_X (see Section 4.2). This profile is represented as a black line in the right panel of Figure 4. We apply the conversion coefficient to the X-ray surface brightness profiles extracted on both the X-ray peak and the large-scale centroid in order to obtain the associated emission-measure profiles:

$$\text{EM}(r) = \int n_e n_p dl. \quad (7)$$

The ICM electron-density profile $n_e(r)$ is estimated from the cluster-emission-measure profile using a forward-fitting Bayesian framework. The cluster electron-density distribution is modeled by a Vikhlinin parametric model (SVM; Vikhlinin et al. 2006) simplified by Mroczkowski et al. (2009) and given by

$$n_e(r) = n_{e0} \left[1 + \left(\frac{r}{r_c} \right)^2 \right]^{-3\beta/2} \left[1 + \left(\frac{r}{r_s} \right)^\gamma \right]^{-\epsilon/2\gamma}, \quad (8)$$

where n_{e0} is the central density of the ICM, r_c is the core radius, and the inner and outer slopes of the profile are given by β and ϵ , respectively. The γ parameter gives the width of the

transition located at a radius r_s at which an additional steepening in the profile occurs. The value of γ is fixed at three since it provides a good fit of all of the cluster profiles considered in the analysis of Vikhlinin (2006). We assume the ionization fraction of a fully ionized plasma with an abundance of $0.3Z_\odot$, i.e., $n_e/n_p = 1.199$ (Anders & Grevesse 1989) in order to estimate the proton-density profile in Equation (7). We perform a Markov Chain Monte Carlo (MCMC) analysis to estimate the best-fit value of the five free parameters of the SVM model given the cluster-emission-measure profiles measured on both the X-ray peak and the large-scale centroid. This allows us to estimate the best-fit parameters that maximize the following Gaussian likelihood function:

$$\begin{aligned} -2 \ln \mathcal{L}_{\text{X-ray}} &= \chi_{\text{CXO}}^2 \\ &= \sum_{i=1}^{N_{\text{bin}}} [(\text{EM}_{\text{CXO}} - \widetilde{\text{EM}}) / \Delta \text{EM}_{\text{CXO}}]_i^2 \end{aligned} \quad (9)$$

where N_{bin} is the number of bins in the emission-measure profile EM_{CXO} estimated from the Chandra data with uncertainties given by $\Delta \text{EM}_{\text{CXO}}$, and $\widetilde{\text{EM}}$ is the model of the emission-measure profile obtained from the integration of the SVM profile along the line of sight. The best-fit electron-density profile along with its error bars are estimated from the Markov Chains after ensuring their convergence and applying a burn-in cutoff discarding half of the samples at the beginning of each chain.

6.1.2. Results

The fitted emission-measure profiles are compared with the data in Appendix A. We do not find any significant emission-measure residuals if the X-ray peak is used as the deprojection center. A 3σ residual is found in the annulus containing the X-ray peak if we use the X-ray large-scale centroid as the deprojection center. We note however that the ICM density model defined in Equation (8) is adapted to fit the extracted profiles from the cluster core up to the detection radius.

The density profiles estimated from the analysis of the emission-measure profiles obtained on the X-ray peak and the X-ray large-scale centroid are shown in the left panel of Figure 6 in purple and green, respectively. The density distributions are very well constrained from the cluster core up to $0.7R_{500}$. The density values at radii larger than ~ 600 kpc are obtained without significant constraints. We highlight this in the figure using a vertical dashed line showing the 3σ detection radius in the Chandra data. As the density estimates obtained beyond this radius are only extrapolations from the SVM model, we choose to focus our study in the radius range $r < 0.7R_{500}$. We observe a significant impact of the choice of deprojection center on the estimate of the ICM density distribution in the cluster core. There is an order-of-magnitude difference between the density estimates measured at 10 kpc from the X-ray peak and the X-ray large-scale centroid of MOO J1142+1527. This is due to the peculiar morphology of the cluster hosting its highest-density core at ~ 100 kpc from the large-scale centroid (see Section 5). Both density profiles are however fully compatible at $r \gtrsim 300$ kpc from the chosen deprojection center.

These results show the limit of a 1D analysis to describe the core dynamics of disturbed galaxy clusters. Indeed, if we assume the cuspsiness $\alpha \equiv |d \log(n_e) / d \log(r)|$ to be a good

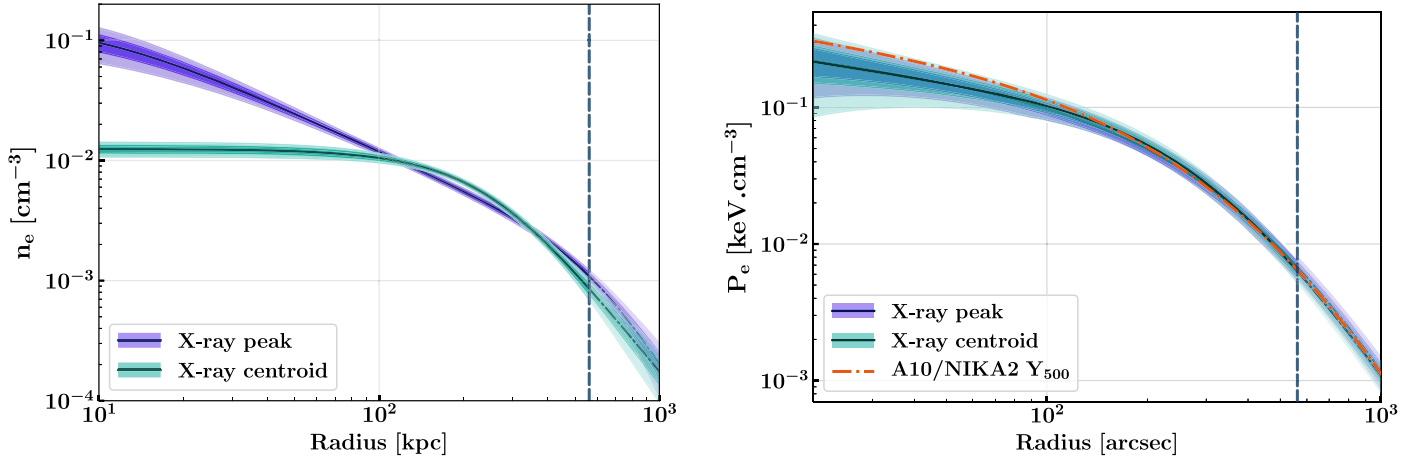


Figure 6. Left panel: density profiles estimated from the analysis of the Chandra X-ray emission-measure profile using a simplified Vikhlinin parametric model (SVM; Vikhlinin et al. 2006). Right panel: pressure profiles obtained from the deprojection of the NIKA2 SZ observations using a generalized Navarro–Frenk–White model (gNFW; Nagai et al. 2007). The orange profile gives the expected pressure profile using the universal pressure profile and scaling relation of Arnaud et al. (2010) along with the NIKA2 estimate of Y_{500} . In both panels, the deprojection center is chosen to be the X-ray peak (purple) or the X-ray centroid (green). The dark lines give the NIKA2 and Chandra best-fits, and the dark and light colored regions represent the 68% and 95% confidence regions on the ICM radial profiles, respectively. We highlight the position of the 3σ detection radius of 562 kpc in the NIKA2 and Chandra data with a vertical dashed blue line and show the best-fit extrapolations in the outer regions with dashed–dotted lines.

proxy to estimate the core dynamics of MOO J1142+1527 (Vikhlinin et al. 2007), this cluster can either host a cool core ($\alpha_{\text{peak}} = 0.95$) or a disturbed core ($\alpha_{\text{centroid}} = 0.04$) depending on the deprojection center that we choose. In the following, we will consider the profiles measured with respect to the X-ray peak to describe the core dynamics, and the ones centered on the large-scale centroid to estimate the integrated quantities such as Y_{500} .

6.2. NIKA2 Pressure Profile

The Chandra data do not allow us to estimate the ICM pressure profile of MOO J1142+1527 because the photon statistics are too low to measure a well-defined temperature profile using X-ray spectroscopy (see Section 4.2). However, the NIKA2 SZ map at 150 GHz enables us to directly measure the pressure distribution of the cluster (see Section 2.1). In this section, we describe the analysis procedure that we used to constrain the pressure profile and present our results.

6.2.1. Method

We use the pipeline developed for the NIKA2 SZ large program (Perotto et al. 2018) and detailed in Ruppin et al. (2018) in order to estimate the pressure profile of MOO J1142+1527. The cluster pressure distribution is modeled by a generalized Navarro–Frenk–White model (gNFW; Nagai et al. 2007), given by

$$P_e(r) = \frac{P_0}{\left(\frac{r}{r_p}\right)^c \left(1 + \left(\frac{r}{r_p}\right)^a\right)^{\frac{b-c}{a}}}, \quad (10)$$

where a defines the width of the transition between the inner and the outer slopes c and b , P_0 is a normalization constant, and r_p is a characteristic radius. All of these parameters are freely varying in an MCMC analysis performed to estimate the best-fit pressure profile of MOO J1142+1527 given the NIKA2 SZ map at 150 GHz and the integrated Compton parameter

measured by CARMA, i.e., $Y_{500} = (9.7 \pm 1.3) \times 10^{-5} \text{ Mpc}^2$ (Gonzalez et al. 2015).

At each step of the analysis, the pressure profile is integrated along the line of sight to obtain a Compton parameter map model. The latter is convolved with a $17''.7$ FWHM Gaussian kernel and with the analysis transfer function (see Section 2.2) to account for the small- and large-scale signal filtering in the NIKA2 data. The filtered Compton parameter map is converted into an SZ surface brightness map model using a conversion coefficient obtained by integrating the SZ spectrum within the NIKA2 bandpass at 150 GHz. Relativistic corrections are applied to the SZ spectrum based on the results of Itoh et al. (1998) using a temperature profile obtained by combining the Chandra density profile (see Section 6.1) and the pressure profile. We model the radio-source signal with a 2D Gaussian model centered at the position found in the FIRST survey. We fix the Gaussian FWHM to the NIKA2 angular resolution at 150 GHz and let the amplitude \tilde{F} vary within a Gaussian prior based on the estimate obtained from the SED fit in Section 3. The SZ map model \tilde{M} , obtained from the sum of the cluster and radio-source signals, and the corresponding integrated Compton parameter \tilde{Y} are finally compared with the NIKA2 and CARMA data using the following Gaussian likelihood:

$$\begin{aligned} -2 \ln \mathcal{L}_{\text{SZ}} &= \chi_{\text{NIK A2}}^2 + \chi_{\text{CARMA}}^2 + \chi_{\text{radio}}^2 \\ &= \sum_{i=1}^{N_{\text{pixels}}^{\text{NIK A2}}} [(M_{\text{NIK A2}} - \tilde{M})^T C_{\text{NIK A2}}^{-1} (M_{\text{NIK A2}} - \tilde{M})]_i \\ &\quad + \left[\frac{Y_{500} - \tilde{Y}}{\Delta Y_{500}} \right]^2 + \left[\frac{F_{150 \text{ GHz}} - \tilde{F}}{\Delta F_{150 \text{ GHz}}} \right]^2 \end{aligned} \quad (11)$$

where $M_{\text{NIK A2}}$ and $C_{\text{NIK A2}}$ are the NIKA2 SZ surface brightness map and noise covariance matrix, respectively, at 150 GHz, and Y_{500} is the CARMA integrated Compton parameter measured with the uncertainty ΔY_{500} . As the raw data analysis method detailed in Section 2.2 has allowed us to measure an almost flat noise power spectrum in the NIKA2 map at 150 GHz, the pixel-to-pixel correlation induced by residual-correlated noise in the NIKA2 map is negligible compared to the rms noise within each pixel at this frequency.

We therefore assume that the NIKA2 χ^2 is given by

$$\chi_{\text{NIKA2}}^2 = \sum_{i=1}^{N_{\text{pixels}}^{\text{NIKA2}}} [(M_{\text{NIKA2}} - \tilde{M})/M_{\text{RMS}}]_i^2 \quad (12)$$

where M_{RMS} is the map of the rms noise in each pixel of the NIKA2 map at 150 GHz. It is computed from simulated noise maps including the instrumental, atmospheric, and astrophysical contaminants (see Section 2.3). The fact that we do not need to use a noise covariance matrix at 150 GHz to account for the residual noise properties at this frequency allows us to decrease the computation time of the likelihood value at each step of the MCMC from 0.2 s to 0.5 ms. We compute the best-fit pressure profile and its associated error bars from the samples remaining in the Markov Chains after their convergence and a burn-in cutoff discarding the first 50% of each chain.

6.2.2. Results

We compare the SZ surface brightness profiles extracted from the data and best-fit model maps in Appendix A. The residuals detected in the maps are also shown in the lower panels of the figure. Although no significant residual is detected by subtracting the best-fit SZ surface brightness profiles to the data, we find $>3\sigma$ positive and negative signals in the SZ map residuals obtained by considering both the X-ray peak and the X-ray large-scale centroid as deprojection centers. These residuals are very significant if the X-ray peak is considered because the latter is located ~ 150 kpc to the east of the NIKA2 SZ peak (cyan diamond in Figure 5). As the X-ray large-scale centroid is only ~ 50 kpc away from the SZ peak, the residuals found in the map are much less significant in this case. We note that using the SZ peak as the deprojection center allows us to obtain a residual map with no significant positive signal, but the southwest negative substructure is always detected at 5σ . Using this deprojection center in the joint analysis would, however, lead to even larger residuals in the X-ray analysis (see Section 6.1.2). The comparison between the residuals found with the SZ surface brightness profiles and the SZ map highlights the limits of the spherical cluster hypothesis for such a disturbed system.

The pressure profiles obtained by using both the X-ray peak and the X-ray large-scale centroid as deprojection centers are shown in the right panel of Figure 6 in purple and green, respectively. As the SZ signal has been mapped by NIKA2 up to similar angular scales as the X-ray signal measured by Chandra, we are also able to estimate the pressure profile from the cluster core up to $0.7R_{500}$. As explained in Section 6.1.2, we distinguish the results obtained at larger radii using dashed-dotted lines because they are overconstrained by the model. The two pressure profiles estimated from this analysis are fully compatible, although the deprojection centers are quite different. This comes from the fact that the highest-SZ signal amplitude is measured over a very extended region that encloses both the X-ray peak and the X-ray large-scale centroid (see Section 5). For this reason, the inner slope of the pressure profile does not depend significantly on the deprojection center if the latter is chosen within the closed region delimited by the orange line in Figure 5.

In contrast, the flux of the radio source has a significant impact on the pressure-profile estimate in the cluster core. If we consider the X-ray large-scale centroid as the deprojection

center, the SZ signal is almost azimuthally symmetric, and a gNFW model provides a good description of the cluster morphology observed in the NIKA2 map at 150 GHz. The best-fit value of the radio-source flux at the end of the MCMC is found to be $\tilde{F} = (1.6 \pm 0.1)$ mJy, which is consistent with the expected flux from the source SED (see Section 3). However, if we use the X-ray peak as the deprojection center, the SZ signal is not azimuthally symmetric because of the overpressure region located to the west of the X-ray peak. Furthermore, in this case, the SZ peak position in the map model matches the one of the radio source. For these reasons, the radio-source flux tends to be overestimated in order to maximize the SZ signal amplitude to its west in the SZ map model. Thus, the best-fit value of the radio-source flux in this analysis is found to be $\tilde{F} = (2.2 \pm 0.2)$ mJy, which is more than 2σ higher than the expected flux from the source SED. In order to avoid biasing the estimate of the pressure distribution in the cluster core when using the X-ray peak as the deprojection center, we fix the radio-source flux to its expected value, i.e., $\tilde{F} = 1.5$ mJy in the corresponding MCMC. The inner slope of the estimated profile (in purple in Figure 6) is then fully compatible with the one measured using the X-ray large-scale centroid.

We compare our pressure-profile estimates with the universal pressure profile from Arnaud et al. (2010) scaled to the same integrated Compton parameter (see Section 6.5). The profile is shown with the orange dashed-dotted line in the right panel of Figure 6. We do not find any significant deviations from the shape of the universal pressure profile except for a slightly shallower inner slope. Although a single cluster analysis cannot be used to draw conclusions on the redshift evolution of the ICM pressure distribution, it is interesting to note that the pressure profile of this disturbed cluster at very high redshift is compatible with the mean profile estimated from the study of an X-ray-selected sample at $z < 0.2$ (Arnaud et al. 2010).

6.3. Gas Temperature, Entropy, and Cooling Time

The combination of the Chandra density profile and NIKA2 pressure profile allows us to estimate the other ICM thermodynamic properties of MOO J1142+1527 without relying on X-ray spectroscopy.

Under the ideal-gas assumption, the ICM temperature profile and the Voit entropy parameter²³ profile are estimated from the following equations:

$$k_{\text{B}}T_e(r) = \frac{P_e(r)}{n_e(r)} \quad \text{and} \quad K_e(r) = \frac{P_e(r)}{n_e(r)^{5/3}}, \quad (13)$$

where k_{B} is the Boltzmann constant. We show the temperature and entropy profiles obtained from the combination of the Chandra density profile (see Section 6.1) and NIKA2 pressure profile (see Section 6.2) in Figure 7. We use the same color scheme as the one considered in Figure 6 in order to differentiate the profiles measured using the X-ray peak (purple) and the X-ray large-scale centroid (green) as deprojection centers.

The temperature profiles (left panel) estimated with these two deprojection centers are significantly different at radii $r \lesssim 100$ kpc. We measure a monotonically decreasing temperature from the X-ray centroid up to $0.7R_{500}$. The central

²³ We will call this parameter “entropy” for the remainder of the paper.

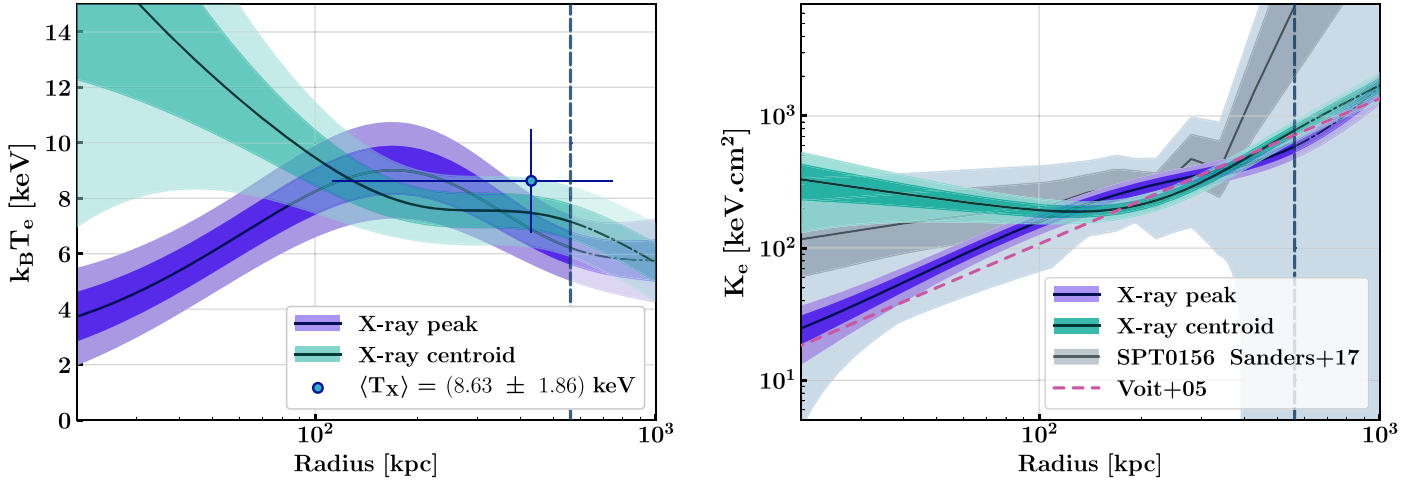


Figure 7. Left panel: temperature profiles estimated from Equation (13) using the combination of the NIKA2 pressure profiles and Chandra density profiles. The temperature radial distributions are compared with the single-point temperature measurement from the Chandra spectroscopy data in the radius range $0.15R_{500} < r < R_{500}$. Right panel: entropy profiles estimated using the results of the NIKA2 and Chandra analyses. We compare our results with the entropy profile of the cluster SPT CLJ0156-5541 at redshift $z = 1.22$ (in gray) estimated from a Chandra-only analysis based on a slightly higher number of X-ray photon counts (Sanders et al. 2017). We also display the self-similar expectation computed from the non-radiative simulation of Voit et al. (2005) with a pink dashed line. In both panels, we use the same color code as in Figure 6 to distinguish the profiles estimated using the X-ray peak and the X-ray centroid as the deprojection center. The unconstrained regions are shown as in Figure 6.

temperature around the SZ peak reaches high values around 14 keV within the enclosed region defined in Figure 5 (orange line). However, the profile estimated by considering the X-ray peak has the typical shape expected for a cool-core cluster. The temperature increases from a low central value of ~ 4 keV up to a maximum of 9 keV at 170 kpc from the X-ray peak. It then decreases at larger radii. These profiles estimated from the combination of X-ray and SZ results are also compatible with the mean ICM temperature estimated from the Chandra spectroscopic data (blue point). We emphasize the large leap forward that such a joint analysis of SZ and X-ray data allows us to make on the characterization of the ICM temperature profile at $z > 1$. Indeed, having a precise measurement of the central temperature, the inner slope of the profile, and the location of the maximum temperature value with X-ray spectroscopy would require an increase of the Chandra exposure of at least an order of magnitude.

The entropy profiles estimated from the combination of the NIKA2 and Chandra results are shown in the right panel of Figure 7. The outer slopes of both profiles are compatible with the self-similar expectation obtained from non-radiative simulations and are shown with a pink dashed line (Voit et al. 2005). However, the radial distribution of the gas entropy estimated by using the X-ray peak is significantly different from the one obtained with the large-scale centroid at $r \lesssim 100$ kpc. We measure a flat entropy distribution at a high value of ~ 230 keV cm² around the X-ray centroid. This is consistent with the disturbed ICM activity at the location of the SZ peak (see Section 5). On the other hand, the entropy profile estimated using the X-ray peak is monotonically increasing from a low central value of ~ 25 keV cm² at 20 kpc from the deprojection center up to ~ 600 keV cm² at $0.7R_{500}$. This profile is consistent with the one expected for a cool-core cluster in which the central radiative cooling is balanced by the activity of the radio-loud AGN detected within the BCG. The central entropy value estimated from this profile depends on the flux of the radio source considered in the NIKA2 MCMC analysis. A flattening of the radio-source SED at high frequency (e.g., Hogan et al. 2015) would indeed result in a

higher expected flux at 150 GHz and, therefore, to a higher central value of the deprojected pressure distribution from the NIKA2 data. However, we have checked that the central entropy value is always lower than ~ 70 keV cm² if we consider a point-source flux lower than 4 mJy at 150 GHz. This shows that the existence of a cool core at the position of the X-ray peak holds even if the radio-source flux at frequencies $\nu > 100$ GHz remains at the same value measured by CARMA at 31 GHz.

Finally, we compare our constraints on the entropy profile of MOO J1142+1527 with the results obtained by Sanders et al. (2017) from the analysis of Chandra data measured on the cluster SPT CLJ0156-5541 at $z = 1.22$ (gray profile). A refined analysis based on the assumption of an underlying dark-matter potential enabled these authors to estimate an entropy profile with a total of 2300 X-ray counts. However, the comparison of this profile with baseline entropy distributions extracted from simulations is difficult because of the large error bars associated with this estimate. Here, we show that a joint analysis combining a slightly lower number of X-ray counts (see Section 4) with high angular resolution SZ observations results in a highly constrained entropy profile even at $z > 1$.

We further describe the properties of the cluster cool core by computing the isochoric cooling time and freefall time profiles given by

$$t_{\text{cool}}(r) = \frac{3(n_e + n_p)k_B T_e}{2n_e n_p \Lambda(T_e, Z)} \quad \text{and} \quad t_{\text{ff}}(r) = \sqrt{\frac{2r}{g(r)}}, \quad (14)$$

where $g(r) = G \cdot B \cdot M_{\text{HSE}}(r)/r^2$ is the gravitational acceleration caused by the total mass $B \cdot M_{\text{HSE}}(r)$ within a sphere of radius r , and G is the gravitational constant. The hydrostatic bias $B = 1/(1-b)$ is a correction applied to the hydrostatic mass profile $M_{\text{HSE}}(r)$ to account for the departure of the gas dynamical state from hydrostatic equilibrium. We use the same ionization fraction considered in Section 6.1 in order to estimate the proton-density profile $n_p(r)$ from the electron-density distribution $n_e(r)$ obtained by considering the X-ray

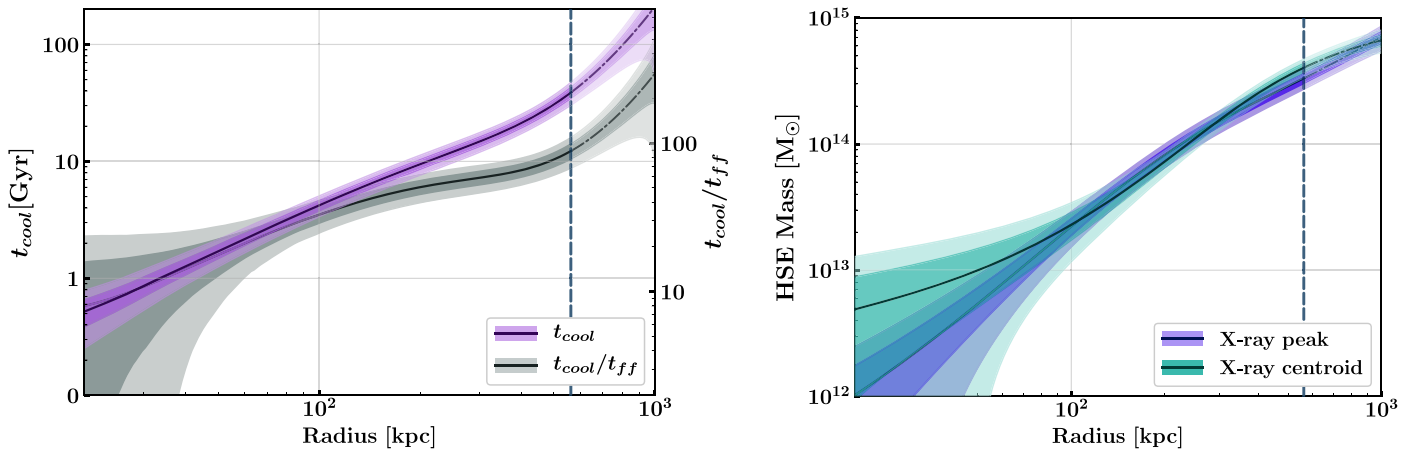


Figure 8. Left panel: profiles of the ICM cooling time (magenta) and of the ratio of the cooling to freefall times (gray) estimated from the density, temperature, and hydrostatic mass profiles issued from the joint analysis of the NIKA2 and Chandra data using the X-ray peak as the deprojection center. Right panel: hydrostatic mass profiles estimated from Equation (15) using the density and pressure profiles deprojected with respect to the X-ray peak (purple) and the X-ray centroid (green). In both panels, the black line gives the best-fit estimate, and the dark and light regions show the 1σ and 2σ confidence regions. The unconstrained regions are shown as in Figure 6.

peak as a deprojection center. Furthermore, we use the cooling function estimated by Sutherland & Dopita (1993) for an optically thin plasma with a $0.3Z_{\odot}$ metallicity to compute $\Lambda(T_e, Z)$ from the temperature profile centered on the X-ray peak, shown in Figure 7. The freefall time is estimated by using the hydrostatic mass profile computed from the combination of the Chandra density and NIKA2 pressure profiles (see Section 6.4 below). We use a hydrostatic bias parameter fixed to $b = 0.2$, following the results of numerical simulations and the comparisons between weak lensing and SZ/X-ray cluster-mass estimates (see, e.g., Figure 10 in Salvati et al. 2018). The cooling-time profile as well as the ratio $t_{\text{cool}}/t_{\text{ff}}$ are represented in the left panel of Figure 8 in magenta and gray, respectively. We measure a cooling time at 20 kpc from the X-ray peak location of $t_{\text{cool}} = (0.51 \pm 0.13)$ Gyr. This is compatible with the distribution of central cooling times estimated by McDonald et al. (2013) on a sample of SPT-selected cool-core clusters. We note that this central cooling time is fairly low given the cluster redshift. This supports the results shown in Figure 6 of McDonald et al. (2013) on the absence of significant redshift evolution of the gas cooling properties in cluster cores. We measure a ratio $t_{\text{cool}}/t_{\text{ff}} \simeq 9$ at the core of MOO J1142+1527. The relationship between the minimum value of $t_{\text{cool}}/t_{\text{ff}}$ and the central entropy is therefore consistent with the distribution measured on the sample of X-ray selected clusters at a mean redshift $\langle z \rangle = 0.17$ dubbed the Archive of Chandra Cluster Entropy Profile Tables (ACCEPT; Voit & Donahue 2015). In summary, although MOO J1142+1527 displays many features of a morphologically disturbed galaxy cluster (see Section 5) at a redshift $z = 1.2$, its core properties are very similar to those observed in typical cool-core clusters at low redshift.

6.4. Hydrostatic Mass and Compton Parameter

The estimates of both the density and pressure profiles of MOO J1142+1527 allow us to infer the total mass of this cluster independently of any scaling relation calibrated at lower redshifts. We estimate the total mass enclosed within a radius r

Table 2
Estimates of the R_{500} Radius, Hydrostatic Mass (M_{500}), and Integrated Compton Parameter (Y_{500}) Computed from the Combination of the Chandra Density and NIKA2 Pressure Profiles

	X-Ray Centroid	X-Ray Peak
R_{500} [kpc]	841 ± 31	812 ± 41
M_{500} [$\times 10^{14} M_{\odot}$]	6.06 ± 0.68	5.49 ± 0.85
Y_{500} [$\times 10^{-4}$ arcmin 2]	2.95 ± 0.21	2.96 ± 0.23

Note. The values estimated by considering both the X-ray centroid and peak emission as deprojection centers are compared.

under the hydrostatic equilibrium assumption:

$$M_{\text{HSE}}(r) = -\frac{r^2}{\mu_{\text{gas}} m_p n_e(r) G} \frac{dP_e(r)}{dr}, \quad (15)$$

where m_p is the proton mass and $\mu_{\text{gas}} = 0.61$ is the mean molecular weight of the gas. The hydrostatic mass profiles computed from the density and pressure profiles estimated by using the X-ray peak and the X-ray large-scale centroid as deprojection centers are both represented in the right panel of Figure 8 in purple and green, respectively. The profiles are compatible with each other from the cluster core up to $0.7R_{500}$; although, the inner slope of the profile measured from the X-ray centroid is shallower than the one obtained at the X-ray peak. The hydrostatic mass profile of MOO J1142+1527 is used to compute its density-contrast profile $\langle \rho(r) \rangle / \rho_c$, where $\rho(r) = M_{\text{HSE}}(r) / V(r)$, $V(r)$ is the cluster volume at a radius r , and ρ_c is the critical density of the universe at $z = 1.2$. This allows us to directly measure the value of R_{500} . The estimates of R_{500} measured from the two mass profiles enable us to compute the total mass of the cluster M_{500} as well as its integrated Compton parameter Y_{500} . The results are summarized in Table 2.

The results obtained with the two mass profiles are all compatible within their 1σ confidence intervals. The error bars associated with the estimates derived from the mass profile measured using the X-ray peak are, however, larger than the ones obtained with the X-ray centroid. A spherical model is

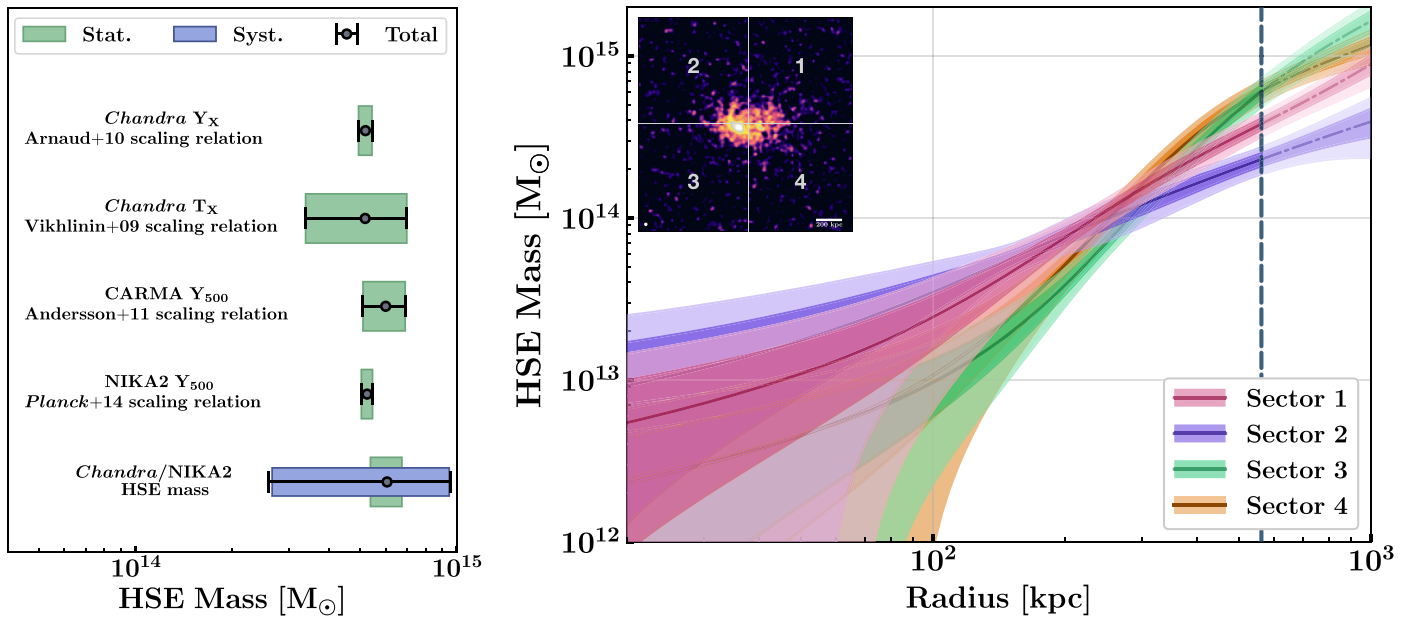


Figure 9. Left panel: comparison of the mass estimates of MOO J1142+1527 obtained from the Chandra Y_X and T_X observables and the CARMA/NIKA2 integrated Compton parameters Y_{500} , along with scaling relations calibrated at low redshift with the hydrostatic mass value estimated from the combination of the Chandra density profile and NIKA2 pressure profile centered on the X-ray centroid. Statistical uncertainties are shown in green while the systematic uncertainty of the hydrostatic mass estimate (in blue) is obtained from the scatter between the mass profiles shown in the right panel. Right panel: hydrostatic mass profiles obtained from the combination of the NIKA2 pressure profiles and Chandra density profiles extracted in four different angular sectors centered on the large-scale X-ray centroid, shown in the inset map of the Chandra X-ray surface brightness. Each mass profile is labeled with a number corresponding to the considered angular sector. The unconstrained regions are shown as in Figure 6.

indeed ill-suited to subtract the extended emission to the west of the X-ray peak without creating strong residuals to its east in both Chandra and NIKA2 data. While using the X-ray centroid as the deprojection center induces residuals around the X-ray peak because the X-ray signal is not azimuthally symmetric in this area, the extended emission is subtracted with more accuracy in this case. More quantitatively, the minimum χ^2 value obtained at the end of the NIKA2 MCMC analysis (see Section 6.2) is decreased by 11% if we use the X-ray centroid instead of the X-ray peak as the deprojection center. Although considering the X-ray peak as the deprojection center is mandatory to have an accurate description of the cluster core properties (see Section 6.3), using the X-ray centroid leads to both more accurate and more precise estimates of the integrated quantities of MOO J1142+1527 such as M_{500} and Y_{500} . We therefore discuss the results obtained with the X-ray centroid as follows.

The R_{500} radius measured with this multiwavelength analysis is compatible with the estimate based on the measurement of the mean ICM spectroscopic temperature and the $M_{500}-T_X$ relation from Vikhlinin et al. (2009; see Section 4.1). Moreover, our estimate of M_{500} is fully compatible with the value determined by Gonzalez et al. (2015) using the CARMA integrated Compton parameter along with the Andersson et al. (2011) $Y_{500}-M_{500}$ scaling relation, i.e., $M_{500}^{\text{CARMA}} = (6.0 \pm 0.9) \times 10^{14} M_{\odot}$. Based on our measurement of the integrated Compton parameter of MOO J1142+1527 computed from the spherical integral of the NIKA2 pressure profile up to R_{500} , we estimate the expected mass of this cluster using the Planck scaling relation (Planck Collaboration et al. 2014): $M_{500}^{\text{Planck}} = (5.25 \pm 0.21) \times 10^{14} M_{\odot}$. The cluster mass reported in Table 2 is therefore compatible with the scaling-relation-based value given the error bars of our estimate and the intrinsic scatter associated with the Planck scaling relation

calibrated at redshifts $z < 0.45$. In addition, we compute the pseudo-integrated Compton parameter $Y_X = M_{g,500} \times T_X$ using the gas-mass measurement $M_{g,500}$ obtained by integrating the Chandra density profile centered on the X-ray centroid and the mean spectroscopic temperature found in Section 4.2. We estimate the total mass of the cluster using the $M_{500}-Y_X$ scaling relation of Arnaud et al. (2010) and find $M_{500}^{Y_X} = (5.19 \pm 0.25) \times 10^{14} M_{\odot}$. Based on all of these different mass estimates, we therefore confirm that MOO J1142+1527 is the most massive galaxy cluster known to date at $z > 1.15$ from an analysis based on spherical models of the ICM density and pressure distributions and the assumption of hydrostatic equilibrium. We compare all mass estimates of this cluster given in this paper in the left panel of Figure 9. We highlight that our hydrostatic mass estimate obtained by combining the deprojected ICM pressure and density profiles is compatible with the ones computed based on the mass-observable scaling relation calibrated using low-redshift cluster samples.

6.5. Systematic Error on the Hydrostatic Mass

As shown in Section 5, MOO J1142+1527 is not a relaxed cluster, nor can it be considered spherical given the precision of the Chandra and NIKA2 measurements (see Appendix A). Thus, we perform a dedicated analysis in order to estimate a systematic uncertainty caused by both the expected departure of the cluster dynamical state from hydrostatic equilibrium and the modeling error induced by the use of a spherical model to deproject the ICM pressure and density distributions.

We analyze both the Chandra and NIKA2 observations in four angular sectors of 90° opening angles centered on the large-scale X-ray centroid (see inset in the right panel of Figure 9). The density and pressure profiles are estimated in each of these sectors following the methodology described in

Sections 6.1 and 6.2. We use Equation (15) to compute the mass profiles based on these results assuming that the ICM is in hydrostatic equilibrium in each sector and that its thermodynamic properties can be described by spherically symmetric distributions. If the cluster was perfectly spherical and morphologically relaxed, these four mass profiles would be compatible at all scales. We represent the hydrostatic mass profiles estimated in each sector in Figure 9. Although these profiles are compatible in the cluster center, we measure significant discrepancies at radii larger than ~ 400 kpc. We consider these differences as an indicator of the systematic error associated with the estimate of the total mass of the cluster. As the outer slopes and amplitudes of the four profiles are different, the values of R_{500} estimated from the radial distribution of the density contrast in each sector are also significantly different. Therefore, we choose to define the systematic uncertainty associated with our estimate of the hydrostatic mass of this cluster as the standard deviation between the mass values measured with each profile at a radius of 841 kpc, i.e., the R_{500} estimate given in Table 2. We also measure the mean of these four mass values to define a new estimate of the cluster total mass. The hydrostatic mass of MOO J1142+1527 obtained by this analysis is given by $M_{841 \text{ kpc}} = (7.4 \pm 3.4) \times 10^{14} M_{\odot}$. Although this result is fully compatible with the hydrostatic mass estimate given in Table 2, we emphasize that the dispersion of the mass estimates between the four angular sectors is three times higher than the error bar associated with the mass measurement at 841 kpc in each sector. Our final estimate of the hydrostatic mass of MOO J1142+1527 is given by the measurement referenced in Table 2 along with this additional systematic uncertainty: $M_{500} = (6.06 \pm 0.68^{\text{stat}} \pm 3.40^{\text{syst}}) \times 10^{14} M_{\odot}$. Although the disturbed dynamical state of MOO J1142+1527 is not striking from the visual inspection of the NIKA2 map at 150 GHz, this multiwavelength analysis has shown that the precision of the mass measurement of this particular cluster is not limited by the noise properties in the Chandra and NIKA2 data but by our modeling of the ICM thermodynamic properties.

The knowledge of the systematic uncertainty on M_{500} induced by an incorrect modeling of the ICM properties is essential to perform an accurate calibration of the mass-observable scaling relation. This analysis highlights the importance of the combination of SZ and X-ray observations to accurately measure the dynamical properties of high-redshift galaxy clusters. Furthermore, it shows that a 1D modeling of the ICM is intrinsically unsuited to describe the true distributions of the thermodynamic properties of morphologically disturbed clusters. In this context, mapping the average value of the gas properties along the line of sight can provide new insights into the dynamical state of such unrelaxed systems.

7. Spatially Resolved Maps of ICM Properties

7.1. Method

Mapping the ICM temperature in disturbed clusters using X-ray spectroscopic data has led to a better understanding of the complex processes occurring in sloshing (e.g., Calzadilla et al. 2019) or merging (e.g., Million & Allen 2009) systems. However, the realization of such maps usually requires thousands of X-ray counts per resolution element in order to have a precise measurement of the relative difference between

the temperature estimates in each region of the map. Mapping the ICM temperature of MOO J1142+1527 from its core up to a large fraction of R_{500} based only on X-ray spectroscopic measurements would therefore require more than 1 Ms of exposure with Chandra or XMM-Newton even with a very coarse binning of the map.

The different dependencies of the X-ray and SZ surface brightness with respect to the distribution of density and temperature along the line of sight allow us to combine the Chandra and NIKA2 data at the pixel level in order to map all of the ICM thermodynamic properties of MOO J1142+1527 without relying on X-ray spectroscopy. We follow the methodology described in detail in Adam et al. (2017b) in order to estimate the maps of the ICM pressure (\bar{P}_e) and density (\bar{n}_e) distributions averaged along the line of sight based on the NIKA2 and Chandra data:

$$\bar{P}_e(\alpha, \delta) = \frac{1}{\ell_{\text{eff}}} \int P_e dl = \frac{m_e c^2 y_{\text{tSZ}}}{\sigma_T \ell_{\text{eff}}} \quad (16)$$

$$\bar{n}_e(\alpha, \delta) = \frac{1}{\ell_{\text{eff}}} \int n_e dl = \frac{1}{\sqrt{\ell_{\text{eff}}}} \sqrt{\frac{4\pi (1+z)^4 S_X}{\Lambda(T_e, Z)}} \quad (17)$$

where y_{tSZ} and S_X are the NIKA2 Compton parameter map and Chandra X-ray surface brightness map, respectively, and ℓ_{eff} is the map of the effective electron depth given by

$$\ell_{\text{eff}} = \frac{\left(\int n_e dl\right)^2}{\int n_e^2 dl}. \quad (18)$$

This map provides an estimate of the line-of-sight extension of the ICM in each pixel. We follow the procedure introduced by Adam et al. (2017b) and compute two estimates of this map based on the ICM density profiles obtained using the X-ray peak and X-ray centroid as deprojection centers. Thus, these maps give an estimate of the effective path length in a more resolved way than the global result issued from the method pioneered in Mroczkowski et al. (2012). The uncertainty associated with the estimate of ℓ_{eff} is dominated by the departure of the ICM geometry from the spherical model used in this analysis. We favor the X-ray peak instead of the X-ray centroid to compute the final maps $\bar{P}_e(\alpha, \delta)$ and $\bar{n}_e(\alpha, \delta)$ because our goal is to accurately map the ICM thermodynamic properties of MOO J1142+1527 in the core area. However, we compute the uncertainties associated with these maps using both estimates of ℓ_{eff} . The two ℓ_{eff} maps considered in this analysis are shown in Figure 10. We measure a minimum effective electron depth of ~ 500 kpc at the X-ray peak in the ℓ_{eff} map obtained using the density profile centered on the X-ray peak. The cluster extent increases toward the outskirts and reaches a value of ~ 1400 kpc at $1'$ from the X-ray peak.

The Compton parameter map measured by NIKA2 is deconvolved from the transfer function in order to minimize the bias induced by the large-scale filtering of the SZ signal. We estimate the standard deviation in each pixel of the pressure map by computing two samples of 1000 realizations of \bar{P}_e using NIKA2 noise maps also deconvolved from the transfer function instead of y_{tSZ} in Equation (16) and the two realizations of ℓ_{eff} . We also take into account the effect of the point-source subtraction in the Compton parameter map by simulating

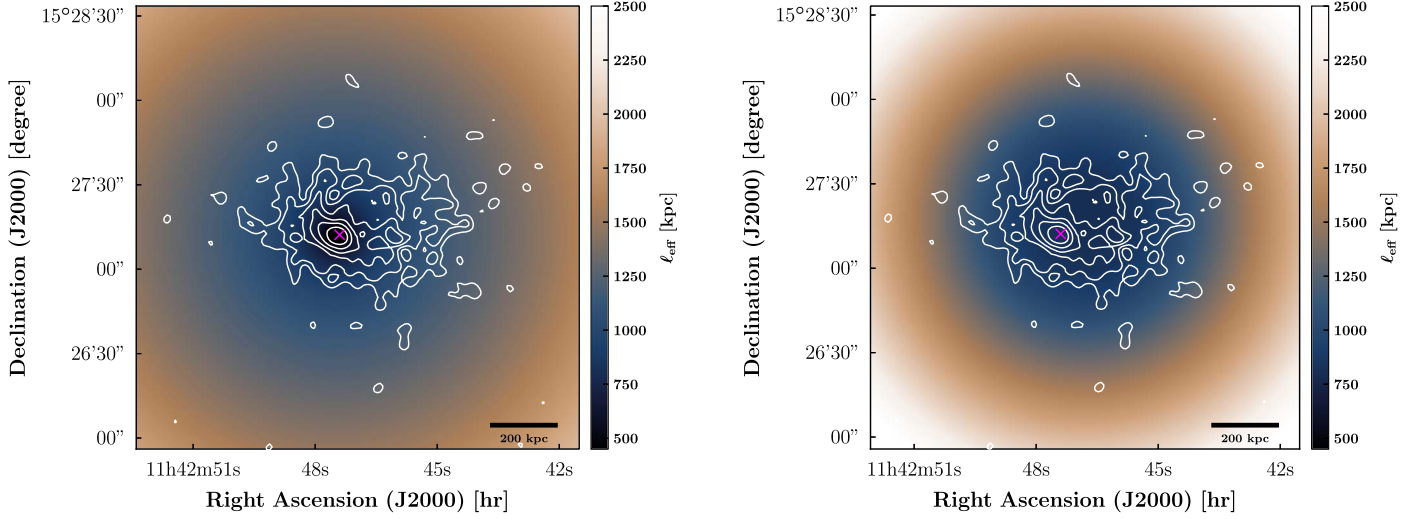


Figure 10. Maps of the effective electron depth ℓ_{eff} computed with the density profiles estimated using the X-ray peak (left panel) and the X-ray centroid (right panel) as deprojection centers. The Chandra surface brightness contours are shown in white, and the magenta cross displays the location of the X-ray peak.

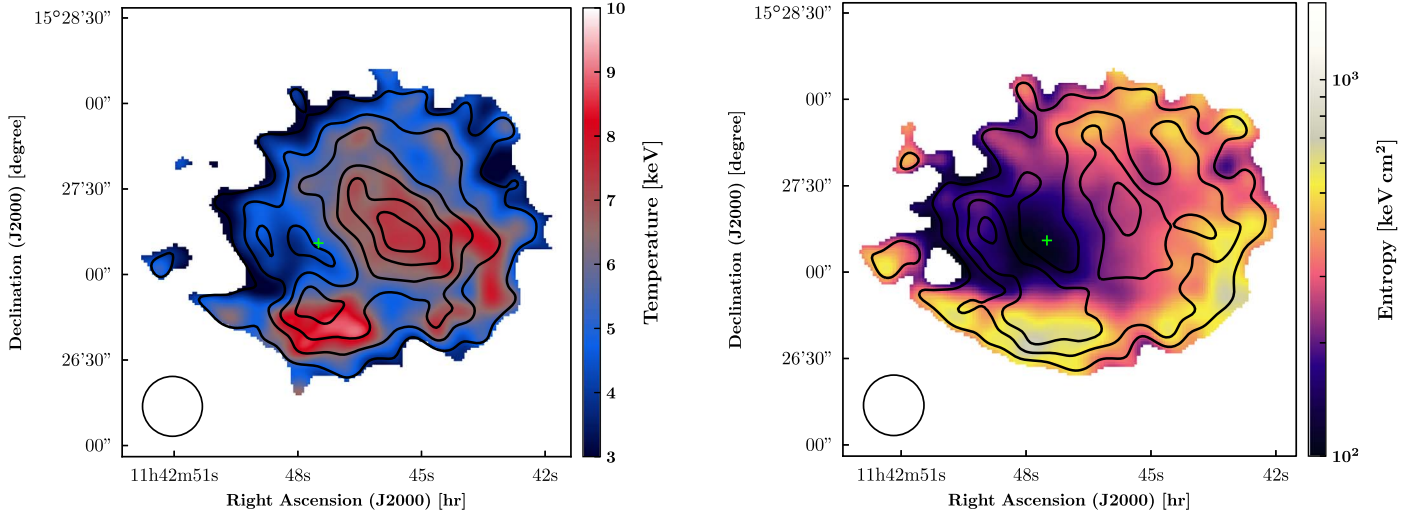


Figure 11. Temperature (left panel) and entropy (right panel) maps of MOO J1142+1527 obtained from the combination of the pressure and density maps of the ICM measured with the NIKA2 and Chandra data, respectively; see Equations (16) and (17). The S/N contours shown in black start at a value of 3σ , increasing in steps of 1σ . We only show the estimated temperature and entropy values in the regions where the S/N is higher than 2.

different realizations of y_{tSZ} marginalizing over the radio-source flux given the constraints obtained in Section 3.

The Chandra map is corrected for vignetting and then processed through an adaptive filter using the CIAO `csmooth` routine. This allows us to produce a map where the minimum angular scales match the effective angular resolution of $20''$ adopted for the \bar{P}_e map and where the minimum S/N is equal to 3. Several realizations of this filtered map are made by taking into account the Poisson fluctuations of the X-ray signal and shuffling the pixel values of the X-ray background map before subtracting it from the Chandra surface brightness map. We use these S_X realizations along with the two ℓ_{eff} ones in order to compute two samples of 1000 realizations of \bar{n}_e maps from Equation (17).

The temperature and entropy maps of MOO J1142+1527 are estimated from the combination of the pressure- and density-map realizations:

$$k_B \bar{T}_e = \bar{P}_e / \bar{n}_e \quad \text{and} \quad \bar{K}_e = \bar{P}_e / \bar{n}_e^{5/3}. \quad (19)$$

The results obtained by using the ℓ_{eff} map computed with the ICM density profile centered on the X-ray peak are shown in both panels of Figure 11. We indicate the location of the BCG with a green cross. The signal-to-noise contours estimated from the knowledge of the temperature and entropy fluctuations in each pixel from the 2000 realizations of the \bar{P}_e and \bar{n}_e maps are shown with black lines, with the lower contour at 3σ . The error maps obtained from the \bar{P}_e and \bar{n}_e map realizations and used to compute these S/N contours are shown in Appendix B. We measure the spatial distribution of the ICM temperature and entropy up to a distance of $0.5R_{500}$ from the cluster centroid. We emphasize that the S/Ns on these temperature and entropy estimates take into account the effect of the differences between the two density profiles estimated in Section 6.1 on the ℓ_{eff} map. We show the distributions of the temperature values obtained in the core and in the southwest regions of the cluster from the Monte Carlo realizations of temperature maps computed by using the two estimates of ℓ_{eff} in Figure 12. As

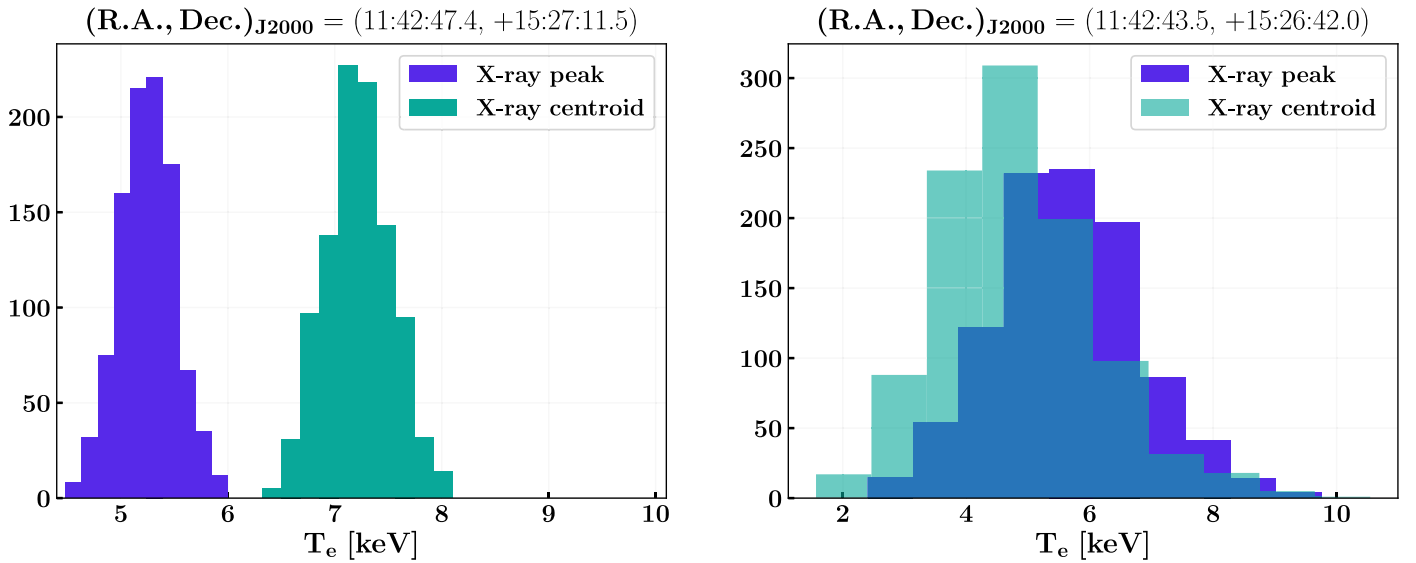


Figure 12. Distributions of the Monte Carlo realizations of the estimates of ICM temperature averaged along the line of sight measured in the core (left panel) and in the southwest (right panel) regions of MOO J1142+1527. The distributions in purple (green) show the temperature values measured on the maps obtained by using the ℓ_{eff} map estimated from the density profile centered on the X-ray peak (X-ray centroid).

the density estimates given at the location of the X-ray peak by the two profiles shown in Figure 6 are significantly different, the two distributions of the core temperature shown in the left panel are consequently different. This explains why the S/N on the core temperature and entropy values shown in Figure 11 is much weaker than the one reached in the intermediate regions of the cluster where the temperature and entropy values obtained with the two estimates of ℓ_{eff} are fully compatible (see right panel of Figure 12). This highlights the high degeneracy between the error maps and the considered ℓ_{eff} map. Using both estimates of the ℓ_{eff} map (see Figure 10) to compute the realizations of \bar{P}_e and \bar{n}_e enables taking part of this degeneracy into account to estimate the S/N contours shown in Figure 11.

7.2. Results

A prominent feature, particularly in the entropy map shown in Figure 11, is the significant detection of a cool core at the location of the BCG. The temperature measured at this location is at least two times lower than the one observed in the surrounding regions, and the entropy is three times lower than the mean entropy value measured in the whole map. Furthermore, the core appears to be well-delimited. The core entropy averaged along the line of sight is enclosed between 100 and 200 keV cm^2 within a circular region extending over a ~ 120 kpc radius from the BCG. We measure a significant increase of the ICM temperature to the west of the BCG. This feature is consistent with the merging scenario described in Section 5 as we expect the gas within this region to be shock-heated by the infalling subcluster (B) from the northwest to the southeast of the main halo (A). The entropy measured at the location of the infalling galaxy group is slightly lower than the one observed at similar radii from the cluster BCG but in different directions. This could be a hint of the presence of a second core associated with this merging substructure. However, this difference is not significant given the entropy fluctuations at this location.

An interesting feature identified in both maps is the presence of a high-temperature and -entropy region southward of the

BCG location. While the relative difference between the temperature measured in this region and the one observed at the cluster centroid varies between all of the realizations of \bar{T}_e , its absolute value is always twice as high as the one measured in the cool core. The interpretation of this feature is quite challenging given its location with respect to the different structures in the galaxy distribution (see Section 5). There is however a hint of an additional peak in the galaxy distribution observed by Spitzer to the east of the BCG (labeled ‘C’ in Figure 5). If this galaxy group is actually in a post-merger state and has undergone a head-on collision from the southwest regions to its current location, the ICM would have been shock-heated at the collision point during the merging process, and the gas within the substructure would have been stripped away from its potential well. This would explain both the high temperature measured to the south of the X-ray peak and the low gas density observed to the east of the cluster at the location of the galaxy group (C). We note however that deeper observations would be needed to confirm this possible scenario. In particular, higher-exposure X-ray observations would enable measuring the X-ray spectroscopic temperature in the region to the south of the X-ray peak. With our current X-ray data set, the spectrum extracted in this region is well fitted by an absorbed APEC model with $k_B T = 10$ keV ($\chi^2/\text{ndf} = 0.55$) as well as with $k_B T = 5$ keV ($\chi^2/\text{ndf} = 0.52$). An XMM-Newton proposal led by I. Bartalucci, also an author on this paper, has been accepted to map the X-ray emission of MOO J1142+1527 for a total of 105 ks. The larger effective area of XMM-Newton combined with this higher exposure should enable measuring a precise value of the spectroscopic temperature in this region of the cluster.

We emphasize the complementarity between the results of the 1D analysis described in Section 6 and the maps of the ICM thermodynamic properties described in this section to explore the merger dynamics of MOO J1142+1527. To the best of our knowledge, this is the very first time that such a detailed analysis of the ICM has been achieved at $z > 1$. This study paves the way for an in-depth characterization of the ICM

properties of very high-redshift galaxy clusters from a combination of spatially resolved X-ray and SZ observations.

8. Future Analyses

The analysis presented in this paper has demonstrated how shallow X-ray observations of $z > 1$ galaxy clusters can provide state-of-the-art descriptions of the ICM thermodynamic properties once combined with high angular resolution SZ observations. This represents a significant step forward in the characterization of the ICM dynamics at $z > 1$ compared to previous X-ray analyses of SZ-selected clusters that relied on assumptions on the shape of the ICM profiles or on stacking analyses in order to constrain the ICM thermodynamic properties. We are planning to combine the outcome of this work with allocated XMM-Newton data to investigate the large-scale properties of the ICM. In particular, we will compare the XMM-Newton spectroscopic temperature profile of this cluster with the mass-weighted profiles shown in Figure 7. Mapping the X-ray signal at larger radii will also allow us to study the gas clumpiness as well as nonthermal pressure support around R_{500} .

Furthermore, we intend to conduct such a joint analysis of SZ and X-ray data on a sample of high-redshift clusters drawn from the MaDCoWS survey. This will allow us to investigate the redshift evolution of the ICM properties such as the entropy excess above the self-similar expectation and its link with merger activity, map the ICM temperature and study its variations given the presence of radio-loud AGNs or merging substructures, and provide strong evolutionary constraints on the astrophysical processes involved during the most active part of cluster formation.

Five other clusters at $0.93 \leq z \leq 1.75$ from the MaDCoWS and the IRAC Distant Cluster Survey samples have already been observed by Chandra with at least 500 counts in the region of interest (Cycle 14-17-18, PIs: A. Stanford–M. Brodwin). Furthermore, an NIKA2 proposal has been accepted to carry out SZ mapping of these clusters and to reach similar signal-to-noise levels at 150 GHz as the ones measured for MOO J1142+1527. Once these observations are completed, we will be able to provide a description of the mean ICM thermodynamic properties in this sample of six clusters in a range of masses from 2.6 to $6.1 \times 10^{14} M_{\odot}$. The number of objects in this sample will of course need to be increased in order to have more statistically significant results on the redshift evolution of the mean ICM properties with respect to $z < 1$ clusters. Such a pilot study will greatly benefit the forthcoming optical-infrared surveys with the *Euclid* satellite, the Rubin Observatory (formerly LSST; LSST Science Collaboration et al. 2009; Refregier et al. 2010; Euclid Collaboration et al. 2019), and the the Spectro-Photometer for the History of the universe, Epoch of Reionization and Ices Explorer (SPHEREx; Doré et al. 2018) by providing evolutionary constraints on cluster dynamics in the $1 < z < 2$ redshift range based on a multiwavelength analysis combining SZ, X-ray, and infrared data.

9. Summary and Conclusions

We have presented a joint analysis of spatially resolved X-ray and SZ observations of the $z = 1.2$ cluster MOO J1142+1527, combining data sets obtained by Chandra and NIKA2. With a cleaned exposure of 46.2 ks, the number of X-ray

counts in the cluster area is too low to deproject the ICM temperature profile based on spectroscopic data only. However, a joint analysis of the NIKA2 and Chandra data enables us to characterize the ICM thermodynamic properties with unprecedented precision at this redshift. Our main results are summarized below:

1. We find a ~ 100 kpc offset between the location of the X-ray peak and the X-ray large-scale centroid in the Chandra map. Furthermore, the SZ peak location in the NIKA2 map at 150 GHz is found at the frontier between the two peaks in the galaxy distribution mapped by the IRAC instrument on board Spitzer. These two galaxy overdensities are located around the radio-loud BCG at the position of the X-ray peak and in the northwest of the cluster, respectively. The projected large-scale ICM morphology is found to be elliptical, with a main extension of the diffuse emission oriented along the R. A. axis, and with a slight tilt oriented toward the northwest. All of these morphological features are consistent with a merging scenario where a subcluster located in the northwest is interacting with the main halo centered on the BCG.
2. The ICM density and pressure profiles are estimated from a deprojection of the Chandra and NIKA2 data, respectively. We identify a significant impact of the choice of deprojection center on the shape of the density profile estimated from the Chandra data. We conclude that using the X-ray peak is best suited for a measurement of the ICM density at the location of the BCG, whereas the X-ray large-scale centroid is more appropriate to estimate the global gas properties. However, this choice does not have a significant impact on the shape of the pressure profile estimated from the NIKA2 data because of the flat distribution of the SZ signal in the cluster core. Using the X-ray peak as the deprojection center, we measure a cuspliness of the gas density of $\alpha = 0.95$, which indicates the presence of a cool core.
3. We estimate the temperature, entropy, cooling time, and hydrostatic mass profiles without relying on X-ray spectroscopy by combining the Chandra density and NIKA2 pressure profiles. The complementarity between the SZ and X-ray data sets allows us to tightly constrain the shape of all of these ICM profiles from the cluster core up to $0.7R_{500}$. The relative uncertainties on both the temperature and entropy profiles achieved by this joint analysis represent a large leap forward in the characterization of the ICM properties at $z > 1$. The estimated temperature, entropy, and cooling-time profiles are typical of cooling-flow clusters. We measure a temperature drop from 9 keV at 170 kpc from the BCG to 4 keV in the core, a central entropy of ~ 25 keV cm², and a central cooling time of $t_{\text{cool}} = (0.51 \pm 0.13)$ Gyr. Combined with our measurement of the cuspliness and the identification of the BCG with a strong radio AGN at the location of the X-ray peak, these results lead us to the conclusion that MOO J1142+1527 hosts a well-regulated cool core very similar to those observed at low redshifts.
4. We evaluated the systematic uncertainty caused by the spherical modeling of the ICM of this disturbed cluster on its hydrostatic mass estimate. We confirm the high mass of this system but find that the systematic uncertainty is significantly limiting the precision of our measurement:

$M_{500} = (6.06 \pm 0.68^{\text{stat}} \pm 3.40^{\text{syst}}) \times 10^{14} M_{\odot}$. While this uncertainty could be lowered with a better modeling of the ICM, e.g., with a triaxial model of the gas density and pressure distributions, we emphasize the importance of taking it into account when using such a hydrostatic mass estimate to calibrate the mass-observable scaling relation used for cluster cosmology.

5. Taking advantage of the different dependence of the SZ and X-ray signals with respect to the line-of-sight distributions of the ICM density and temperature, we have produced temperature and entropy maps by combining the NIKA2 and Chandra data sets at the pixel level. We clearly identify the cool core within the ICM from a relatively low-entropy value at the position of the BCG. In addition, we confirm the disturbed dynamical state of MOO J1142+1527 from an analysis of the spatial variations in the plane of the sky of these ICM quantities averaged along the line of sight. In particular, we identify a high-temperature region at the interface between the two peaks in the galaxy distribution suggesting that the gas has been shock-heated in this area. A more surprising, yet significant, feature revealed by these maps is the presence of a high-temperature and high-entropy region to the south of the BCG. This increase in temperature may have been induced by the galaxy group identified to the east of the BCG that might have already undergone a first passage with the main halo from south to east. This would explain both the lack of gas at the position of this galaxy group and the temperature excess in the collision region.

This work demonstrates the level of detailed analysis made possible by joint SZ/X-ray analyses on the characterization of the ICM of $z > 1$ clusters, in particular, on the dynamics of mergers and on the core properties. This study paves the way for a systematic analysis of galaxy clusters, during the most active part of their formation history, from the complementarity of current X-ray observatories and the new generation of high angular resolution millimeter instruments. This technique allows us to push the investigation of the ICM evolution to the $z > 1$ regime before the next generation of X-ray observatories such as *Athena* and *Lynx* come into play.

We would like to thank the IRAM staff for their support during the campaigns. The NIKA dilution cryostat has been designed and built at the Institut Néel. In particular, we acknowledge the crucial contribution of the Cryogenics Group,

and in particular Gregory Garde, Henri Rodenas, Jean Paul Leggeri, and Philippe Camus. This work has been partially funded by the Foundation Nanoscience Grenoble and the LabEx FOCUS ANR-11-LABX-0013. This work is supported by the French National Research Agency under the contracts “MKIDS”, “NIKA”, and ANR-15-CE31-0017 and in the framework of the “Investissements d’avenir” program (ANR-15-IDEX-02). This work has benefited from the support of the European Research Council Advanced Grant ORISTARS under the European Union’s Seventh Framework Programme (grant agreement No. 291294). We acknowledge fundings from the ENIGMASS French LabEx (R.A. and F.R.), the CNES post-doctoral fellowship program (R.A.), the CNES doctoral fellowship program (A.R.) and the FOCUS French LabEx doctoral fellowship program (A.R.). R.A. acknowledges support from Spanish Ministerio de Economía and Competitividad (MINECO) through grant No. AYA2015-66211-C2-2. This work has benefited from the support of the European Research Council Advanced Grants ORISTARS and M2C under the European Unions Seventh Framework Programme (grant agreement Nos. 291294 and 340519). Support for this work was provided by NASA through SAO Award Number SV2-82023 issued by the Chandra X-Ray Observatory Center, which is operated by the Smithsonian Astrophysical Observatory for and on behalf of NASA under contract NAS8-03060. This work is based in part on observations made with the Spitzer Space Telescope, which is operated by the Jet Propulsion Laboratory, California Institute of Technology under a contract with NASA.

Appendix A

Comparison of the Projected Models and the Data

We compare the best-fit models of the X-ray emission-measure and SZ surface brightness profiles with the Chandra and NIKA2 data in Figure A1. The left (right) panels show the results obtained by using the X-ray peak (centroid) as the deprojection center. The maps of the SZ residuals measured by subtracting the best-fit models from the NIKA2 surface brightness map at 150 GHz are shown in the bottom panels. The fact that we do not observe significant residuals on the surface brightness profiles but that strong residuals are detected in the SZ map is a clear indication that a spherical model is not adapted to model both the X-ray and SZ signals in such a disturbed system.

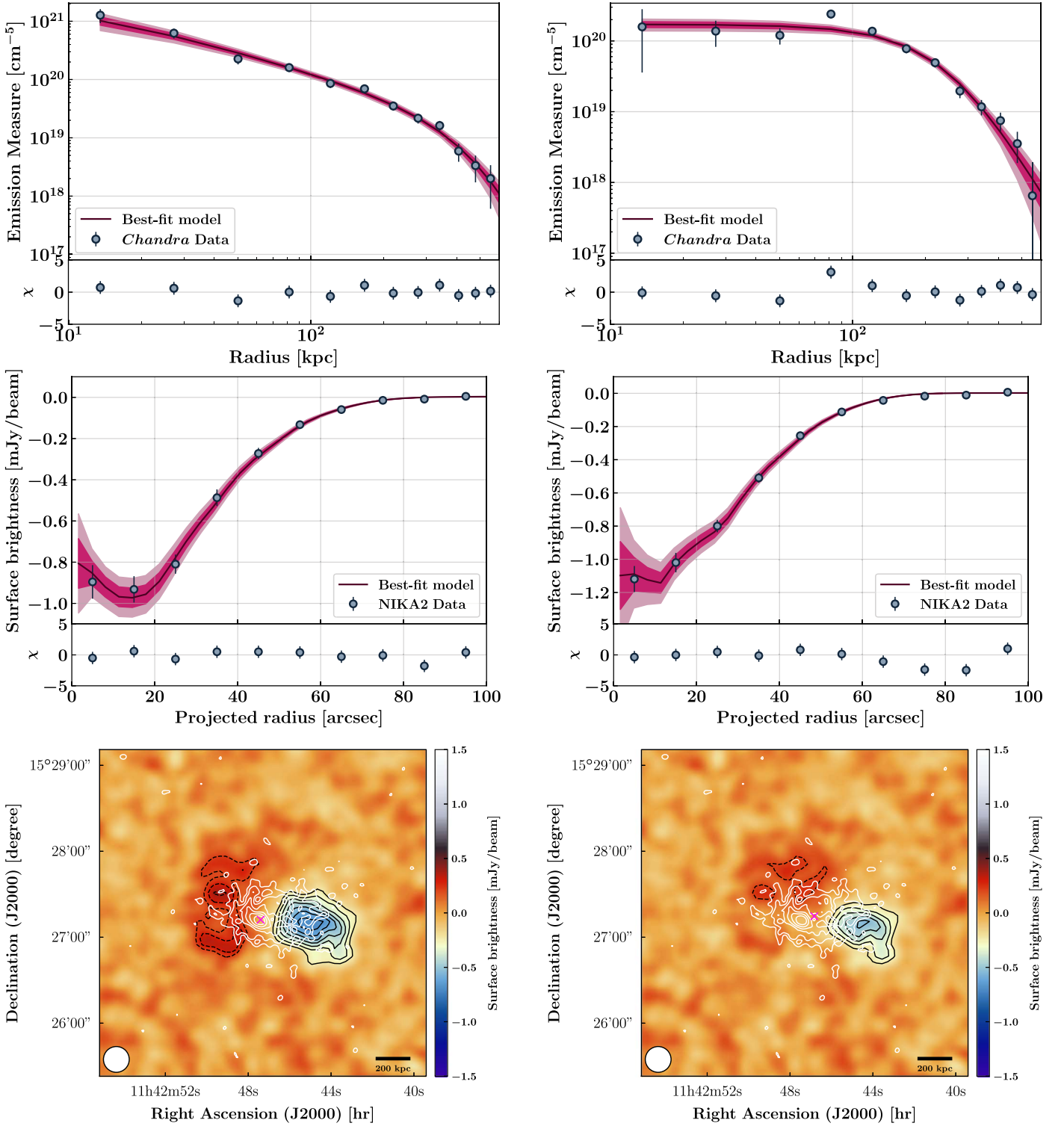


Figure A1. Best-fit X-ray emission-measure profiles (top panels), SZ surface brightness profiles (middle panels), and SZ map residuals (bottom panels) obtained with the joint analysis using the X-ray peak (left panels) and the X-ray centroid (right panels) as the deprojection center. The lower parts of the top and middle figures show the difference between the best-fit models and the data divided by the measurement errors. The significance contours (black) in the SZ residual maps start at a confidence level of 2σ and increase with 1σ steps. The white contours show the distribution of the X-ray signal mapped by Chandra, and the magenta cross shows the location of the considered deprojection center.

Appendix B Temperature and Entropy Error Maps

We show the error maps of the temperature and entropy estimated from the 2000 simulations described in Section 7 in

Figure B1. They have been obtained by computing the standard deviation of the temperature and entropy estimates in each pixel of the 2000 simulations of \bar{T}_e and \bar{K}_e . These maps have been used to compute the S/N contours shown in Figure 11.

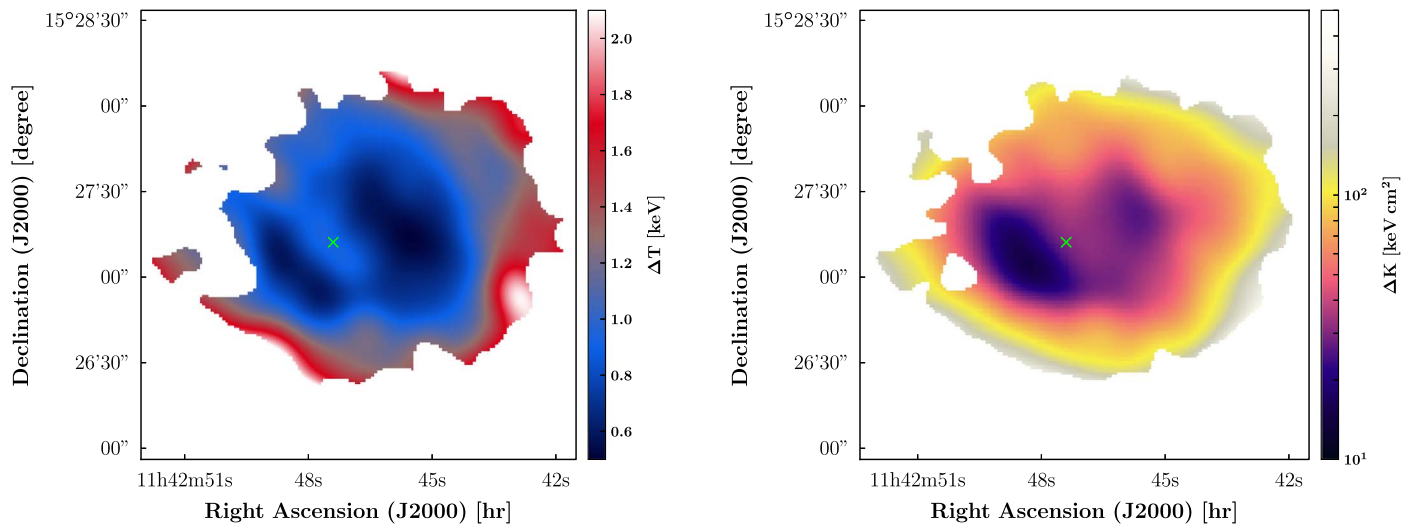


Figure B1. Maps of the uncertainty of the temperature (left panel) and entropy (right panel) measured in each pixel of the maps shown in Figure 11. These uncertainties take into account the noise fluctuations in the NIKA2 and Chandra surface brightness maps as well as the systematic uncertainty induced by the difference between the density profiles considered to compute the ℓ_{eff} map. The green cross shows the location of the X-ray peak.

ORCID iDs

- M. Brodwin <https://orcid.org/0000-0002-4208-798X>
 P. Ade <https://orcid.org/0000-0002-5127-0401>
 A. H. Gonzalez <https://orcid.org/0000-0002-0933-8601>
 E. Moravec <https://orcid.org/0000-0001-9793-5416>
 C. Romero <https://orcid.org/0000-0001-5725-0359>
 D. Stern <https://orcid.org/0000-0003-2686-9241>

References

- Adam, R., Adane, A., Ade, P. A. R., et al. 2018, *A&A*, 609, A115
 Adam, R., Arnaud, M., Bartalucci, I., et al. 2017b, *A&A*, 606, A64
 Adam, R., Bartalucci, I., Pratt, G. W., et al. 2017a, *A&A*, 598, A115
 Adam, R., Comis, B., Bartalucci, I., et al. 2016, *A&A*, 586, A122
 Adam, R., Comis, B., Macías-Pérez, J. F., et al. 2014, *A&A*, 569, A66
 Adam, R., Comis, B., Macías-Pérez, J. F., et al. 2015, *A&A*, 576, A12
 Alberts, S., Pope, A., Brodwin, M., et al. 2016, *ApJ*, 825, 72
 Anders, E., & Grevesse, N. 1989, *GeCoA*, 53, 197
 Andersson, K., Benson, B. A., Ade, P. A. R., et al. 2011, *ApJ*, 738, 48
 Arnaud, K. A. 1996, in ASP Conf. Proc. 101, *Astronomical Data Analysis Software and Systems V*, ed. G. H. Jacoby & J. Barnes (San Francisco, CA: ASP), 17
 Arnaud, M., Pratt, G. W., Piffaretti, R., et al. 2010, *A&A*, 517, A92
 Becker, R. H., White, R. L., & Helfand, D. J. 1995, *ApJ*, 450, 559
 Béthermin, M., Daddi, E., Magdis, G., et al. 2012, *ApJL*, 757, 2
 Birkinshaw, M. 1999, *PhR*, 310, 97
 Bleem, L. E., Stalder, B., de Haan, T., et al. 2015, *ApJS*, 216, 27
 Bourdin, H., & Mazzotta, P. 2008, *A&A*, 479, 307
 Bulbul, E., Chiu, I.-N., Mohr, J., et al. 2019, *ApJ*, 871, 50
 Calvo, M., Benoît, A., Catalano, A., et al. 2016, *JLTP*, 184, 816
 Calzadilla, M. S., Russell, H. R., McDonald, M., et al. 2019, *ApJ*, 875, 65
 Carlstrom, J. E., Holder, G. P., & Reese, E. D. 2002, *ARA&A*, 40, 643
 Chambers, K. C., Magnier, E. A., Metcalfe, N., et al. 2016, arXiv:1612.05560
 Dicker, S. R., Ade, P. A. R., Aguirre, J., et al. 2014, *JLTP*, 176, 808
 Doré, O., Werner, M. W., Ashby, M. L. N., et al. 2018, arXiv:1805.05489
 Eckert, D., Molendi, S., & Paltani, S. 2011, *A&A*, 526, A79
 Euclid Collaboration, Adam, R., Vannier, M., et al. 2019, *A&A*, 627, A23
 Fakhouri, O., Ma, C.-P., & Boylan-Kolchin, M. 2010, *MNRAS*, 406, 2267
 Gonzalez, A. H., Decker, B., Brodwin, M., et al. 2015, *ApJL*, 812, L40
 Gonzalez, A. H., Gettings, D. P., Brodwin, M., et al. 2018, *ApJ*, 240, 33
 Hasselfield, M., Hilton, M., Marriage, T. A., et al. 2013, *JCAP*, 07, 08
 Hogan, M. T., Edge, A. C., Hlavacek-Larrondo, J., et al. 2015, *MNRAS*, 453, 1201
 Intema, H. T., Jagannathan, P., Mooley, K. P., & Frail, D. A. 2017, *A&A*, 598, A78
 Itoh, N., Kohyama, Y., & Nozawa, S. 1998, *ApJ*, 502, 7
 Kalberla, P. M. W., Burton, W. B., Hartmann, D., et al. 2005, *A&A*, 440, 775
 Kitayama, T., Ueda, S., Takakuwa, S., et al. 2016, *PASJ*, 68, 88
 LSST Science Collaboration, Abell, P. A., Allison, J., et al. 2009, arXiv:0912.0201
 Markevitch, M. 2001, *Memo ACIS Background* (Cambridge, MA: Harvard Univ. Press), <http://cxc.harvard.edu/contrib/maxim/bg>
 Markevitch, M., Gonzalez, A. H., Clowe, D., et al. 2004, *ApJ*, 606, 819
 Maughan, B. J., Jones, C., Forman, W., & Van Speybroeck, L. 2008, *ApJS*, 174, 117
 McDonald, M., Allen, S. W., Bayliss, M., et al. 2017, *ApJ*, 843, 28
 McDonald, M., Benson, B. A., Vikhlinin, A., et al. 2013, *ApJ*, 774, 23
 McDonald, M., Benson, B. A., Vikhlinin, A., et al. 2014, *ApJ*, 794, 67
 McDonald, M., Bulbul, E., de Haan, T., et al. 2016, *ApJ*, 826, 124
 McDonald, M., McNamara, B. R., Voit, G. M., et al. 2019, *ApJ*, 885, 63
 Million, E. T., & Allen, S. W. 2009, *MNRAS*, 399, 1307
 Moreno, R. 2010, *Neptune and Uranus Planetary Brightness Temperature Tabulation*, Tech. Rep., (Paris: ESA Herschel Science Center), <ftp://ftp.sciops.esa.int/pub/hsc-calibration/PlanetaryModels/ESA2>
 Mroczkowski, T., Bonamente, M., Carlstrom, J. E., et al. 2009, *ApJ*, 694, 1034
 Mroczkowski, T., Dicker, S., Sayers, J., et al. 2012, *ApJ*, 761, 47
 Mroczkowski, T., Nagai, D., Basu, K., et al. 2019, *SSRv*, 215, 17
 Muldrew, S. I., Hatch, N. A., & Cooke, E. A. 2015, *MNRAS*, 452, 2528
 Nagai, D., Vikhlinin, A., & Kravtsov, A. V. 2007, *ApJ*, 655, 98
 Pacaud, F., Clerc, N., Giles, P. A., et al. 2016, *A&A*, 592, A2
 Perotto, L., Adam, R., Ade, P., et al. 2018, arXiv:1808.10817
 Perotto, L., Ponthieu, N., Macías-Pérez, J. F., et al. 2019, arXiv:1910.02038
 Pike, S. R., Kay, S. T., Newton, R. D. A., et al. 2014, *MNRAS*, 445, 1774
 Planck Collaboration, Ade, P. A. R., Aghanim, N., et al. 2013, *A&A*, 554, A140
 Planck Collaboration, Ade, P. A. R., Aghanim, N., et al. 2014, *A&A*, 571, A20
 Planck Collaboration, Ade, P. A. R., Aghanim, N., et al. 2016a, *A&A*, 594, A24
 Planck Collaboration, Ade, P. A. R., Aghanim, N., et al. 2016b, *A&A*, 594, A27
 Planck Collaboration, Aghanim, N., Akrami, Y., et al. 2018, arXiv:1807.06209
 Pointecouteau, E., Giard, M., & Barret, D. 1998, *A&A*, 336, 44
 Poole, G. B., Babul, A., McCarthy, I. G., et al. 2007, *MNRAS*, 380, 437
 Pratt, G. W., Arnaud, M., Piffaretti, R., et al. 2010, *A&A*, 511, A85
 Press, W. H., & Schechter, P. 1974, *ApJ*, 187, 425
 Refregier, A., Amara, A., Kitching, T. D., et al. 2010, arXiv:1001.0061
 Ruppin, F., Adam, R., Comis, B., et al. 2017, *A&A*, 597, A110
 Ruppin, F., Mayet, F., Macías-Pérez, J. F., & Perotto, L. 2019, *MNRAS*, 490, 784
 Ruppin, F., Mayet, F., Pratt, G. W., et al. 2018, *A&A*, 615, A112
 Salvati, L., Douspis, M., Aghanim, N., et al. 2018, *A&A*, 614, A13
 Sanders, J. S., Fabian, A. C., Russell, H. R., & Walker, S. A. 2017, *MNRAS*, 474, 1065
 Sayers, J., Czakon, N. G., Mantz, A., et al. 2013, *ApJ*, 768, 177

- Smith, R. K., Brickhouse, N. S., Liedahl, D. A., & Raymond, J. C. 2001, *ApJL*, 556, L91
- Sun, M. 2009, *ApJ*, 704, 1586
- Sunyaev, R. A., & Zel'dovich, Y. B. 1972, *CoASP*, 4, 173
- Sunyaev, R. A., & Zel'dovich, Y. B. 1980, *ARA&A*, 18, 537
- Sutherland, R. S., & Dopita, M. A. 1993, *ApJS*, 88, 253
- Tucci, M., Toffolatti, L., de Zotti, G., & Martínez-González, E. 2011, *A&A*, 533, A57
- Vieira, J. D., Crawford, T. M., Switzer, E. R., et al. 2010, *ApJ*, 719, 763
- Vikhlinin, A. 2006, *ApJ*, 640, 710
- Vikhlinin, A., Burenin, R. A., Ebeling, H., et al. 2009, *ApJ*, 692, 1033
- Vikhlinin, A., Burenin, R. A., Forman, W. R., et al. 2007, in *ESO Astrophysics Symp., Heating versus Cooling in Galaxies and Clusters of Galaxies*, ed. H. Böhringer et al. (Berlin: Springer), 48
- Vikhlinin, A., Kravtsov, A., Forman, W., et al. 2006, *ApJ*, 640, 691
- Vikhlinin, A., McNamara, B. R., Forman, W., et al. 1998, *ApJL*, 498, L21
- Voit, G. M., & Donahue, M. 2015, *ApJL*, 799, 1
- Voit, G. M., Kay, S. T., & Bryan, G. L. 2005, *MNRAS*, 364, 909
- Voit, M. 2005, *RvMP*, 77, 207
- Walker, S. A., Fabian, A. C., Sanders, J. S., & George, M. R. 2012, *MNRAS*, 427, L45
- Wright, E. L., Eisenhardt, P. R. M., Mainzer, A., et al. 2010, *AJ*, 140, 1868